MASTER OF SCIENCE THESIS

Bio-inspired inertial sensing by flapping wings

T. L. Mohren B.Sc.

December 15, 2015

Faculty of Aerospace Engineering · Delft University of Technology

Bio-inspired inertial sensing by flapping wings

Master of Science Thesis

For obtaining the degree of Master of Science in Aerospace Engineering at Delft University of Technology

T. L. Mohren B.Sc.

December 15, 2015

Faculty of Aerospace Engineering · Delft University of Technology

Delft University Of Technology
Department Of
Aerodynamics

The undersigned hereby certify that they have read and recommend to the Faculty of Aerospace Engineering for acceptance a thesis entitled **“Bio-inspired inertial sensing by flapping wings”** by **T. L. Mohren B.Sc.** in partial fulfillment of the requirements for the degree of **Master of Science**.

Dated: December 15, 2015

Supervisor
Dr.ir. B.W. van Oudheusden

Co-supervisor
Prof. dr. T.L. Daniel

Reader:
Dr. ir. J.F.L. Goosen

Reader:
Dr. M. Percin

Summary

How hawk moths and many other flying insects acquire information on body rotations outside of the visual system is still unknown. Vision is important for flight stability, but generally believed to be too slow to explain fast reflexes during maneuvers and hovering for species such as the *Manduca sexta*. Insects in the Diptera order (the true flies) acquire angular velocity information with their halteres, club-like organs that once evolved from their hind wings, with strain sensors at their base to detect deformation during turns. The hawk moth wing is richly equipped with strain sensors, but the function of these sensors is still unknown. Could these wing-based strain sensors be used to detect deformation caused by body rotation?

To investigate this hypothesis, an Euler-Lagrange model, a Finite-element model, and a robotic model of a flapping flat plate were subjected to inertial rotations. The difference in strain between the left and the right side of the wing base indicated wing twist in all computational models. Bending strain is two orders larger than the strain due to twist, making experimentally detecting twist challenging. Wing twist was confirmed for three out of four rotation conditions, be it at different frequencies than expected from simulation. Two strain gauges measuring twist at the wing base proved to be capable of detecting wing twist, but not sufficiently robust to act as an angular velocity sensor. Future work could shed light on whether it is in fact the large array of sensors found on insect wings that allows a more robust sensing of wing deformation as a result of inertial rotations.

Acknowledgements

My supervisors have been tremendously supportive and flexible, Dr. van Oudheusden and Prof. Daniel, I thank you sincerely. I would also like to thank my previous supervisors Prof. dr. van Leeuwen and dr. Gussekloo for introducing me to biomechanics and zoology. At no moment was working in the Daniel lab a solitary undertaking. I thank Annika, Brad, Eatai, Dave, Jonathan, Sharri, Octavio, Alison, Elischa, Gideon and Darren for your help and friendship. The Fulbright program and the Netherland-America Foundation, thank you for your financial support, but also for the opportunities you have given me. Kelly and Mary Ann, you have been the most wonderful host family I could have imagined. Anna, Dean, Matt, you have been great roommates. Lastly, I thank my parents Frits and Christien for the freedom and unquestionable support in all that I do.

Contents

Summary **v**

Acknowledgements **vii**

Nomenclature **xi**

Introduction **1**

1 Literature review **3**

1.1 Inertial sensing by insects 3

1.2 Flapping wing kinematics and aerodynamics 9

1.3 Hawk moth wing morphology 16

2 Methodology **21**

2.1 Theory 22

2.2 Model description 25

3 Computational models **27**

3.1 Analytic Euler-Lagrange model 27

3.2 Finite element model 34

4 Experimental setup **37**

4.1 Experiment design 38

4.2 Calibration 40

4.3 Wing eigenfrequency 44

5 Results and discussion **47**

5.1 Constant rotation 49

5.2 Periodic rotation 49

5.3 Evaluation of models 50

5.4 Recommendations 50

Conclusions and significance **53**

References **55**

Appendices **61**

A Coriolis force derivation 61
B Euler-Lagrange derivation 63
C Digital supplement 65

Nomenclature

Latin Symbols

$\bar{c}$	Mean chord length [m]
$\hat{c}$	Non-dimensional chord-wise position [-]
$\hat{r}$	Non-dimensional span-wise position [-]
$\hat{r}_2^2$	Non-dimensional second moment of area [-]
A/D	Analog to digital converter
A_{in}	Analog in pin of the arduino UNO
AR	Aspect ratio [-]
c_m	Mean chord length [m]
C_{Dt}	Empirical calibrated drag coefficient for flapping flight [41] [-]
C_{Lt}	Empirically calibrated lift coefficient for flapping flight [41] [-]
C_L	Lift coefficient[-]
$C_{roth,theo}$	Rotation coefficient [-]
D	Damping]
E	Youngst modulus [kg m^{-2}]
EI	Bending stiffness [Nm^2
f_f	Flapping frequency [Hz]
f_r	Rotation frequency [Hz]
K	Gauge factor
L	Wing length [mm]
m	Wing mass [kg]
N_i	Shape function [-]
NV	Numerical value recorded by an A/D converter
Q_i	Lagrange coefficient
q_i	Shape function coefficient
R	Wing length [m]
Re_{f3}	Reynolds number for flapping wings [-]
S	Wing surface area [m^2]

SR	Sampling rate
T	Kinetic energy [J]
T	Wing thickness [mm]
U_t	Wing tip velocity [ms^{-1}]
V	Potential energy [J]
V_G	Bridge voltage, voltage between two sides of a wheatstone bridge
V_{ex}	Excitation voltage of the wheatstone bridge
W	Wing chord length [mm]
W_1	Angular velocity around body axis 1 sensed by combining information from two halteres [49] [$rads^{-1}$]
W_2	Angular velocity around body axis 2 sensed by combining information from two halteres [49] [$rads^{-1}$]
W_3	Angular velocity around body axis 3 sensed by combining information from two halteres [49] [$rads^{-1}$]

Greek Symbols

α	Angle between haltere stroke plane and the transverse plane [49] [deg]
α	Feathering angle [deg]
δ_i	Local wing deformation [mm]
ϵ	Strain [-]
η	Non-dimensional chordwise location coefficient [-]
μ	Viscosity [m^2s^{-1}]
Ω	Angular velocity [rad s^{-1}]
ω	Absolute angular velocity [$rads-1$]
ω	Vector of body rotations [$\Omega_x, \Omega_y, \Omega_z$]
Ω_b	Angular velocity sensed by the right haltere [49] [$rads^{-1}$]
Ω_c	Angular velocity by the left haltere [49] [$rads^{-1}$]
Φ	Wing stroke amplitude [deg]
ϕ	Wing stroke angle [deg]
ϕ_i	Local span-wise deformation angle [rad]
ρ	Density of air [kgm^{-3}]
θ	Angular position [rad]
θ	Wing elevation angle [deg]
θ_i	Local chord-wise deformation angle [rad]
$\Theta_{Periodic}$	Periodic rotation amplitude [deg]
ξ	Non-dimensional spanwise location coefficient [-]

Subscripts

$1, 2, 3, 4, i$	Node or shape function discrimination
I	Inertial frame
R	Rotational frame

Superscripts

T	Vector transpose

Abbreviations

DAQ	Data acquisition system
ESC	Electronic speed controller
LEV	Leading-edge vortex
MIMU	Micro Inertial Measurement Unit
PIV	Particle image velocimetry

Introduction

Animal flight demonstrates unparalleled levels of performance not seen in artificial systems. Especially at small scale they surpass anything man-made in maneuverability, economy and sensory capabilities. Insects use multimodal sensory integration, driving multiple actuators to masters the complex dynamics demanded of flight. Complex biological control systems like those involved in insect flight can serve as inspiration for robotics and other engineered systems.

Insect vision serves an important role in locomotion planning, mate selection and flight control. However, the visual system is too slow to explain many features of flight, such as rapid maneuvers and flower feeding while hovering by hawk moths. Other than vision, flying insects must thus have another way of acquiring information on their flight state. The insects belonging to the order of the True flies have evolved club-like organs called halteres to measure forces during body rotations, but for other flying insects little is known how flight state is sensed.

Recently the idea has been posed that other sensory richly equipped body parts of insects can sense the effects of the so-called gyroscopic forces, forces resulting from inertial rotations and accelerations. The insect wing is such an organ that is richly embedded with sensors. With over 200 strain sensors on the fore wing of the hawk moth, sensing the additional deformations uniquely present during body rotations could be crucial in the flight control system of the hawk moth.

A similar research has found that twist occurs in flapping flat plates for periodic rotations around one axis [16]. Could twist be the mechanism by which all inertial rotations in the hawk moth are detected? And if so, is there potential to use this mechanism in an engineered system? This thesis investigates these questions with computational and robotic models of flapping wings.

Chapter 1

Literature review

Flapping wing insects such as moths are inherently pitch unstable [21], yet they are capable of maintaining very precise attitude and position (e.g. during feeding). The visual system is inherently slow [29, 48], and although generally insects do not fly without vision, vision alone is not sufficient for controlled flapping flight in most insects. Inertial sensing must thus come from other sensory systems, such as the halteres of Diptera.

1.1 Inertial sensing by insects

The Diptera (and the much smaller order Strepsiptera) possess the club-like organs called halteres (figure 1.1). The literature on the haltere goes back to the early seventeen hundreds, when scientists first found out that halteres were crucial for stable flight in flies. It was not until stroboscopic and electro physiological observations shed light on the haltere that it became firmly established as a sensor for gyroscopic forces [36, 40].

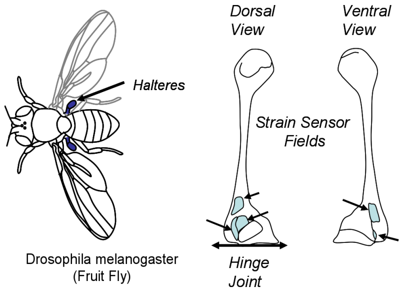

Figure 1.1: The haltere of the fruit fly *Drosophilia melanogaster* [50].

Experiments with fruit flies in a virtual reality environment the haltere was shown to be crucial for flight stability reflexes in all 3 axes of rotation [11]. Ablation of one or both of the halteres resulted in compromised flight stability (figure 1.2).

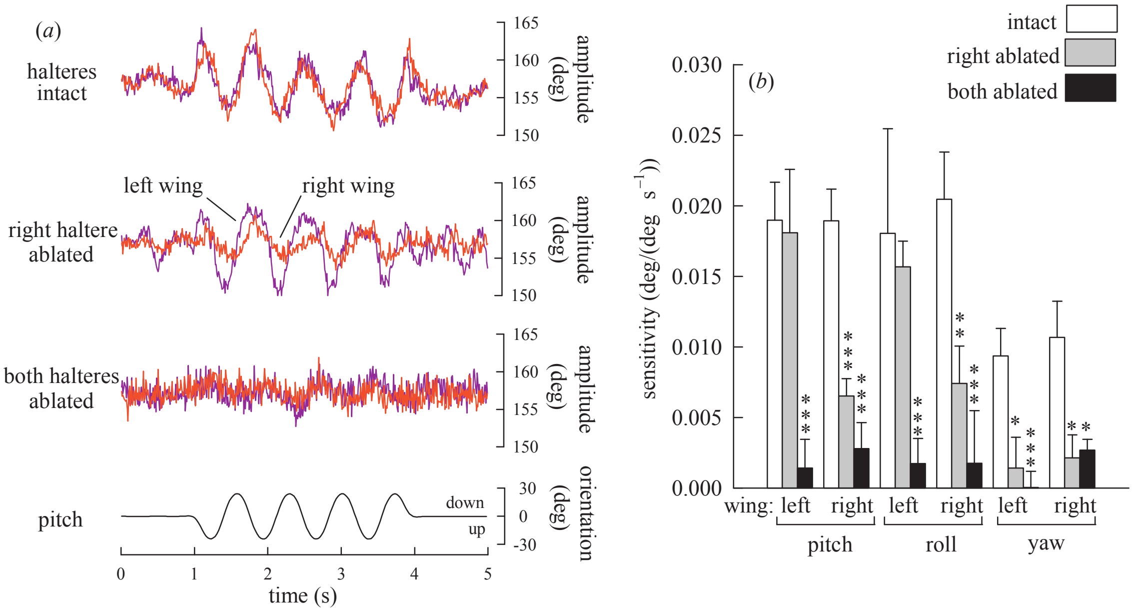

Figure 1.2: (a)The stroke amplitude reflex to a visual pitch stimulus without ablation, with a single haltere ablated, and fully ablated halteres. (b) The sensitivity to input for pitch,roll and yaw stimulus [11].

The fact that flies have two halteres with non equal haltere stroke planes allows them to distinguish between rotation about 3 axes [49]. For a single haltere, a mechanism was defined on how to distinguish both out of plane rotations. The fact that the two stroke planes of halteres each are at an angle α to the transverse plane (figure 1.3) ensures that now all three axes of rotation can be detected. The reference frame consists of axes b_1, b_2, b_3 for the right haltere and c_1, c_2, c_3 for the left. Inertial rotation rate experienced by a haltere about for example axis b_1 is then called Ω_{b_1}.

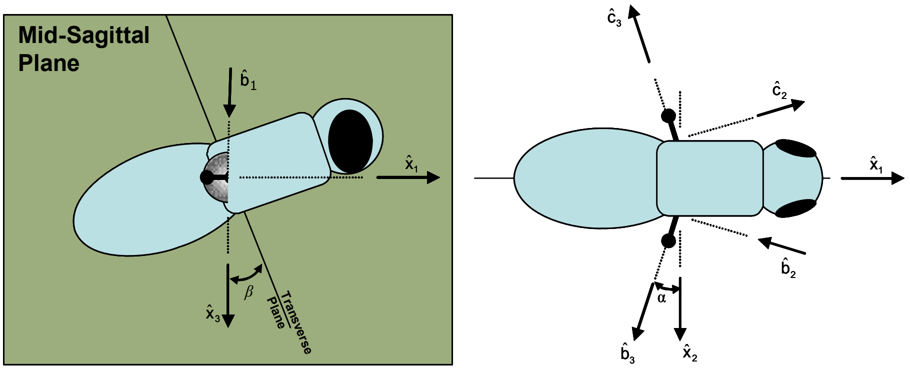

Figure 1.3: The reference frames of the halteres are slanted backwards with respect to the transverse plane by angle α. The reference frame of the left haltere has axes c_1, c_2, c_3, the right haltere has axes b_1, b_2, b_3 [49].

Figure 1.4 shows the forces on the haltere and the out of plane motion during rotation about the three inertial axes $(\hat{x}_1, \hat{x}_2, \hat{x}_3)$. The three inertial rotations (W_1, W_2, W_3), or loosely called roll, pitch and yaw can be distinguished by equations 1.1, 1.2, and 1.3:

$$W_1 = -\frac{\Omega_{b3} + \Omega_{c3}}{2sin(\alpha)} \tag{1.1}$$

$$W_2 = \frac{\Omega_{b3} - \Omega_{c3}}{2cos(\alpha)} \tag{1.2}$$

$$W_3 = -\frac{\Omega_{b1} + \Omega_{c1}}{2} = -\Omega_{b1} = -\Omega_{c1} \tag{1.3}$$

Although we know little on how the downstream neural circuitry works, there are theories on how the neural system could sense angular velocity about the 3 axes of rotation [46, 50].

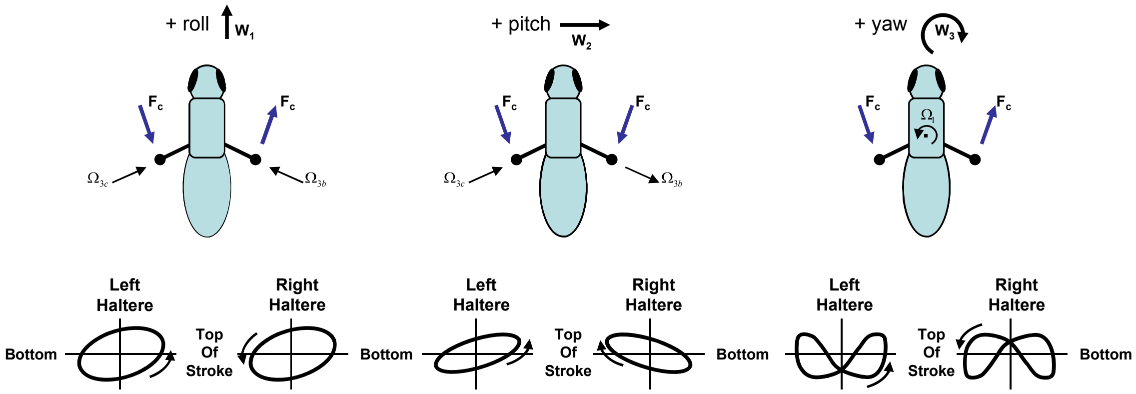

Figure 1.4: Haltere deflection during body rotations. Due to the specific response to each axis of rotation, the model is capable of decoupling the three rotations [49]

Visual system in flight control

Hawk moths have been observed to feed from flowers at night without the presence of moonlight [38], although "they generally do not forage at the dimmest light levels" [48]. The low light conditions and the maintained ability of flight stability question vision as the sole sensory modality for flight control. Furthermore, insect vision is not fast enough to explain the control insects show during rapid maneuvers [29, 48]. Visual stimuli do lead to reflexes by the abdomen of the hawk moth, thereby controlling its attitude in pitch [15].

Gyroscopic force can only be detected during body rotation, thereby only providing sensory information during actual motion. Halteres for example, are crucial in high speed saccades [19]. This supports the case that a gyroscopic organ such as halteres acts as a high-pass filter and vision acts as a low pass filter [2, 43]. The response to mechanical and visual roll stimuli in fruit flies is shown in figure 1.5, where the response to visual stimuli diminishes at higher rates, while the response to mechanical stimuli increases.

However, the two sensory modalities of vision and mechanosensory feedback are not completely separate. Visual input has an effect on the control system of the haltere muscles [6]. Furthermore, when the sensory information is processed in the neurological system, both signals are taken into account. In the fruit fly *Drosophila melanogaster* visual and

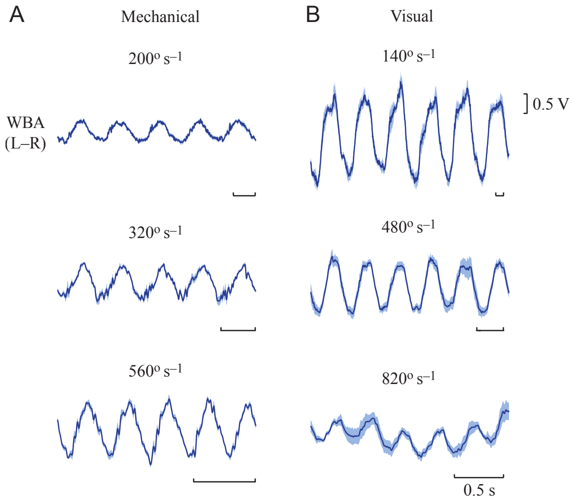

Figure 1.5: The difference of wing beat amplitude (WBA) between the left and right wing as a response to a visual and mechanical roll stimulus in fruit flies, averaged over 9 trials [43].

haltere information are used in determining rotational velocity, their signals are interpreted as a weighted sum [44].

Haltere-inspired inertial sensing

The interest in bio-inspired inertial sensing devices has been limited so far. Mechanical halteres (figure 1.6) have been built and tested in controlled environments, but they have not yet been proven to work in combination with a controller [14, 57]. Even though recent research in Micro Inertial Measurement Units (MIMU) has generated significant cost and size reductions, haltere-like sensors could still yield improvements in range capability [14].

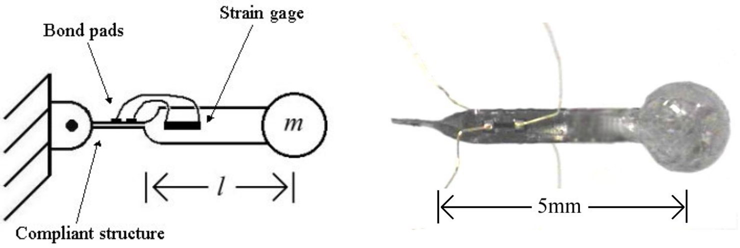

Figure 1.6: The micro-mechanical haltere, flapping at a frequency of 70 Hz [57].

Inertial sensing by the antennae

The antennae of moths are most studied for their olfactory sensing. However, they have a mechanoreceptive organ at the base of their stem that can sense antenna deformations. Until recently these were supposed to be caused by aerodynamic forces alone, but inertial forces may just as well be detected. In flight experiments, ablating one or both antennae led to disrupted flight stability, and subsequently gluing it back on restored flight capabilities [42]. This suggests that among thermo and olfactory sensory capability, the antenna has an important sensory function in flight control.

The antenna is passively vibrated because of wing beating (unlike the halteres, which also have active excitation muscles), resulting in gyroscopic force on the antenna while the insect is rotating. Visual and mechanical rotation stimuli lead to abdominal reflexes in moths, but mechanical body rotations depend on the presence of a fully functioning antenna [24]. The antennae might thus serve a very similar function to that of the haltere. Experiments with a miniature stimulator attached to hawk moth antennal muscles show that stimulations lead to changes in the pitch angle of the animal [25]. Although sensing of gyroscopic forces could very well be responsible for the stability reflexes observed in these experiments, they do not rule out the possibility of aerodynamic feedback on the antennae.

Inertial sensing by the abdomen

The abdomen is known for its role as an actuator in flight stability [21]. However, its continuous actuation means it also perceives gyroscopic forces during body rotations. From strain gauges on a robotic model, the yaw rate of the robot could be extracted, showing that theoretically the abdomen could act as both a sensor and an actuator for flight stability [23].

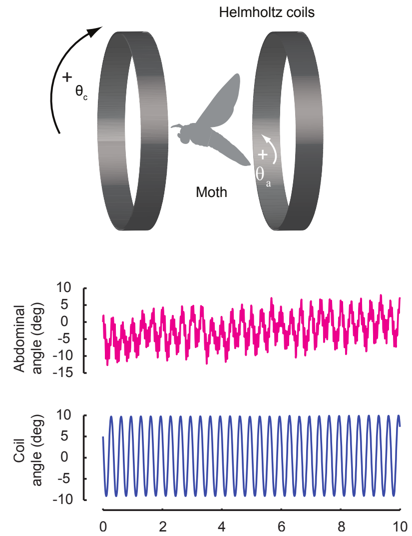

Figure 1.7: The abdomen response of the hawk moth with magnets on its wings to changing orientation of the magnetic field [9].

Inertial sensing by flapping wings

The insect wing has only very recently been considered as a possible inertial sensing organ. Since ablation of wings or numbing nerves to wing campaniforms is not possible, experiments similar to the ablation experiments in flies are out of the question. However, by applying a small magnet on the wing and changing the magnetic field orientation, an abdominal reflex was observed in hawk moths [9]. Figure 1.7 shows the abdomen deflection angle as a response to the change in magnetic field.

Furthermore, with computational and physical models of a flat plate representing a hawk moth wing, body rotational velocity in flapping plastic plates could be extracted by looking at the twisting deformation [16]. This deformation mode could be seen when tracking both free wingtips of the plastic plate (figure 1.8) and by measuring wing strain (figure 1.9).

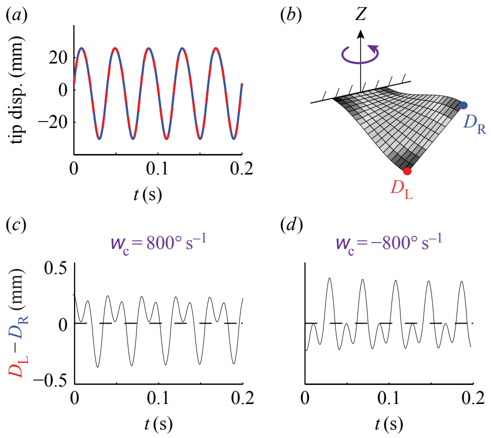

Figure 1.8: The torsional deformation mode caused by Coriolis force at a rotation of 800 $^{o}s^{-1}$. Figure (c) and (d) show the difference in displacement between the left and right free wingtip. Figure from [16].

The concept of inertial sensing by insect wings relies on the ability to sense the presence of small deformations resulting from gyroscopic forces among the much larger deformation due to the flapping motion, and the smaller but not insignificant aerodynamic forces [8]. The Coriolis force depends linearly on inertial rotation rate, and is therefore believed to be the force that allows inertial sensing by halteres, despite it being much smaller than linear acceleration forces in halteres. The Coriolis force is often ignored in engineered systems, and in the case it is studied its effect merely reduces the natural frequency of turbine blades [47]. This study verified earlier assumptions that Coriolis force can generally be ignored for stress calculations on fan blades.

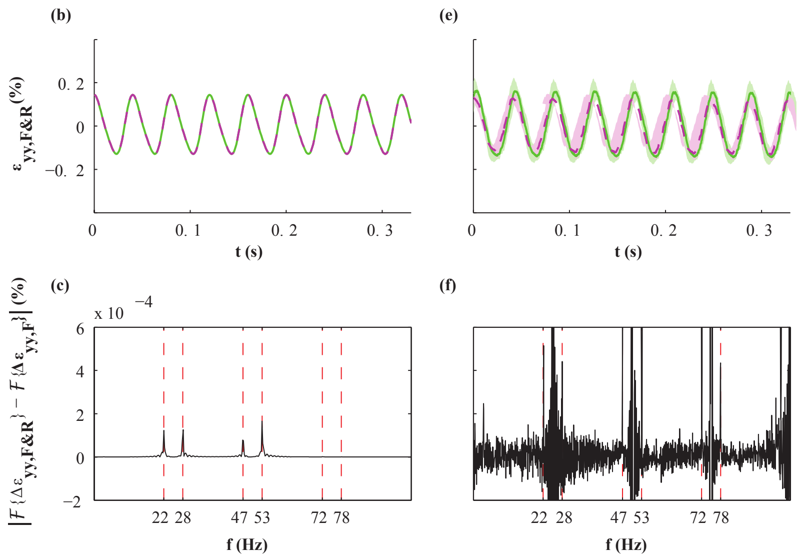

Figure 1.9: The normal strain at the left (solid) and right (dashed) side of the flat plate base for a flapping & rotating wing (F & R). In the computational model, peaks occur in the frequency domain at a 3 Hz offset (the rotational velocity) from the 25 Hz flapping frequency. This is confirmed by the experimental results in the right column. Figure adapted from [16].

1.2 Flapping wing kinematics and aerodynamics

Throughout the insect flight literature there is some variability in the description and naming of flight parameters. The variability of the airframe and an unclear incoming airflow requires an adaptation of the traditional aircraft flight description. Furthermore, the aerodynamic phenomena that have been observed in flapping flight at low Reynolds numbers ($10^1 - 10^4$) are vastly different from the fixed-wing aerodynamics at Reynolds numbers of airplanes.

Inertial frame and wing kinematics

Insect wing motion can be described by rotation about three axes, the wing stroke angle ϕ, the elevation angle θ and the feathering angle α. The feathering angle rarely is constant along the wing, and combined with very flexible wing material connecting the more rigid veins, it is not a trivial parameter to determine. The other two angles are defined by the wing tip position as can be seen in figure 1.10.

The inertial rotations of the insect body are not unambiguous because there is often no forward flight velocity to align an inertial axis with, nor is there a rigid body that is suitable as a reference. Figure 1.10 shows one interpretation of roll/pitch and yaw, but this naming convention is often avoided.

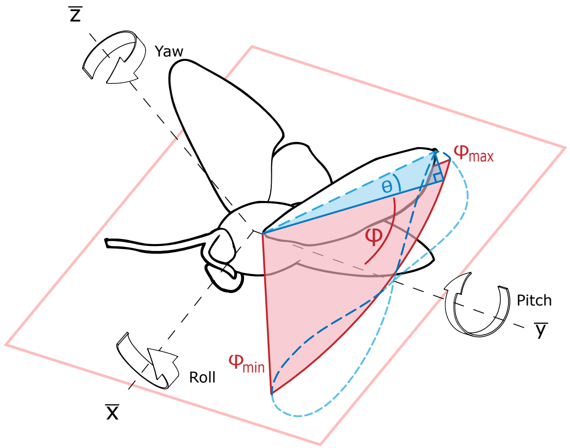

Figure 1.10: The stroke plane is spanned by the wing root and the wing tip at its minimum and maximum stroke angle. The stroke angle ϕ is measured by line spanned from the wingtip to the base of the wing to the $\bar{y}$ axis, and θ is the elevation of that same line from the stroke plane.

The kinematic angles of the hawk moth can be found in figure 1.11. Recent publications on hawk moth wing kinematics also include the feather angle [30, 56] and camber [56]. Note that although in simulations generally the wing stroke angle is assumed to follow a sinusoidal pattern, the observed wing stroke differs significantly.

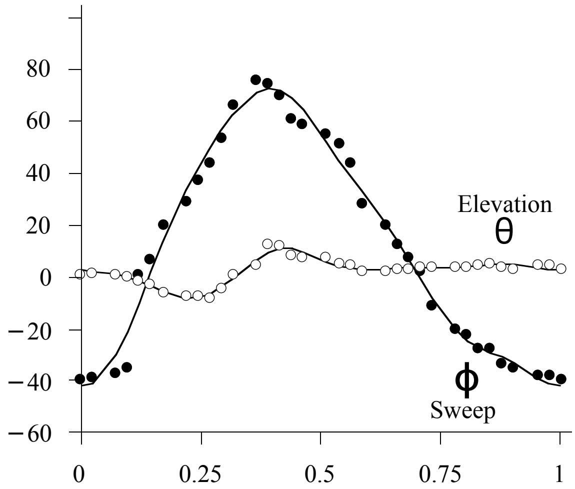

Figure 1.11: The elevation angle θ, and sweep angle ϕ of a hovering hawk moth wing, picture adapted from [54].

Aerodynamics of insect flight

The flow around flapping wings is highly complex. It is a very active field of study from both an experimental and computational perspective. Techniques such as Particle Image Velocimetry (PIV) have provided the scientific community with new insights on the flow patterns in both hovering and forward flight in insects, birds, bats and Micro Aerial Vehicles (MAVs). Furthermore, physical models in denser media such as mineral oil have been used to achieve Reynolds similarity [12, 18, 58]. PIV experiments on physical models of flapping insect wings have played an important role in understanding the complex flow phenomena that occur in hovering flight.

The aerodynamic phenomena observed in hovering flight can be categorized into at least the following categories: i) Leading-edge vortex (LEV), ii) lift peak due to pitch up, iii) wake capture, iv) tip vortex v) clap and fling. More phenomena can be found in the literature, often describing a variation one of the mentioned categories or naming a less obvious effect. In this section phenomena i) to iii) are discussed because I consider them to provide the most insight into hawk moth flight.

The Reynolds number for three dimensional flapping wing, Re_{f3}, can be defined by the wing tip speed, and the averaged chord length. By taking out the average chord length, the Reynolds number can be rewritten to equation 1.5 [45].

$$U_{ref} = 2\Phi f_f R \tag{1.4}$$

$$Re_{f3} = \frac{U_{ref} L_{ref}}{\mu} = \frac{2\Phi f_f R\bar{c}}{\mu} = \frac{2\Phi f_f R^2}{\mu}\left(\frac{4}{AR}\right) \tag{1.5}$$

The flow patterns around flapping wings strongly depend on the Reynolds number [3], and although the flow structures look similar in hawk moths ($Re \sim 5 \cdot 10^3$) and fruit flies ($Re \sim 10^2$), the mechanism that allows the delayed stall to occur is not necessarily the same.

Leading edge vortex

First discovered by Ellington et al. in 1996, the leading edge vortex effect is also referred to as delayed stall [18]. At high angles of attack a vortex appears on the leading edge for the first few chord lengths traveled before the wing stalls. This vortex creates a low pressure area, enhancing lift temporarily. The fact that this delayed stall remains present in the first few chord lengths of travel has been attributed to stabilizing span-wise pressure gradient similar to that of low aspect ratio delta wings, but this has later been disputed [3].

The LEV has been found to occur on the wings of many flying animals. PIV experiments have shown leading-edge vortices on hawk moths [18], hummingbirds [52] bats [34] and swifts [51]. The effect can also be observed with visualization by smoke, LEV have been found in bumblebees this way [5]. Hovering and gliding birds, bats, and insects show this characteristic LEV mechanism.

Numerical simulations of flapping insect flight are in agreement with experimental findings. Vortex structures (figure 1.12) have been observed in unsteady Navier-Stokes computations [31, 32]. With these simulations, it has been possible to confirm experimental results, such as the finding that the downstroke is primarily responsible for lift production in hovering hawk moths, something that was already known for hovering hummingbirds [52].

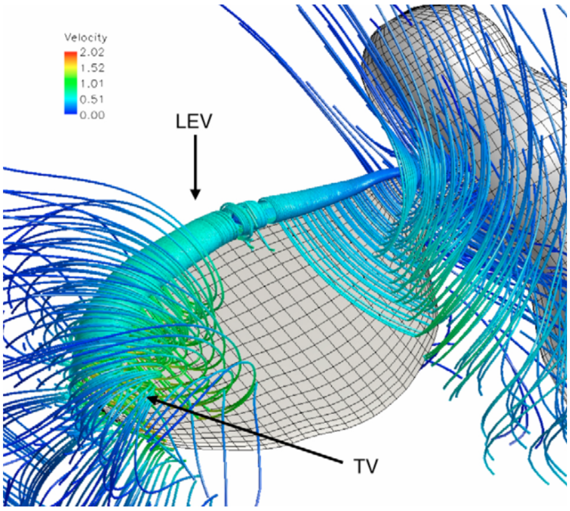

Figure 1.12: The leading edge vortex (LEV) and tip votex (TV) in the numerical simulation of a hovering fruit fly [1].

Rapid pitch up

A rapid increase in angle of attack of an airfoil can greatly enhance lift temporarily [28]. This has also been found to be important in flapping flight [12]. Experiments with advanced and delaying rotation demonstrated that the advanced and symmetrical wing rotations generate superior lift coefficients of 1.74 and 1.64 respectively, the delayed rotation generated a lower C_L of 1.01.

Wake capture

A third enhancement of lift is also attributed to the wing rotation phase. At the start of the translational phase, the flapping wing meets a vortex it generated in its previous translational motion (figure 1.13). This vortex increases the flow velocity, thereby enhancing the lift at the beginning of the wing translation.Even if the wing does not initiate a the translational phase after rotation, the induced velocity from its previously generated vortex will enhance lift temporarily [12].

Quasi-steady aerodynamic theories

There has long been a desire for steady state models of plunging and flapping airfoils. The goal of quasi-steady theories initially was aimed to determine muscle efficiency in hovering

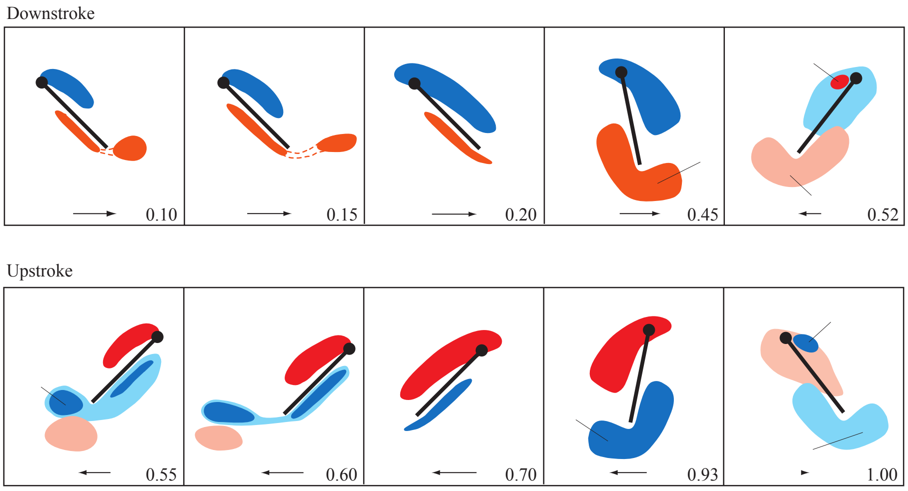

Figure 1.13: A conceptual visualization of the vortex interaction and wake capture during flapping flight. Blue areas represent clockwise vorticity, the red areas represent counter-clockwise vorticity. Adapted from [4].

animals. The actuator disk theory provided a convenient starting point. By taking a circular area with a radius equal to the wing length of the animal the local induced velocity os determined [53]. This model was improved by proposing a partial disk based on the area actually covered by wings during a stroke. Additionally, a correction for the pulsing strength of the disk was applied, based on the presence of vortex rings in the wake [17].

In recent years the goal of the quasi-steady theory has been to obtain instantaneous lift and drag based on the steady state parameters that describe wing motion. From the lift and drag, the span-wise lift and drag coefficients can be estimated with the blade element theory. Using a quasi-steady theory can be very useful to get an indication of the lift and drag coefficients, but to obtain accurate results they still require tuning with experimental data. Early quasi-steady theories have been used to determine the order of magnitude for aerodynamic forces and local pressure coefficients [26].

A quasi-steady model of the aerodynamic forces on the wing of *Drosophila melangaster* was developed by experiments with a scaled wing in mineral oil [41]. The model is based on the decomposition of total instantaneous aerodynamic force (F_{inst}) into four parts (equation 1.6). The quasi-steady force (F_{qs}) takes into account all but the wake-capture term (equation 1.7).

$$F_{inst} = \underbrace{F_a}_{Added\ mass} + \underbrace{F_{trans}}_{LE\ vortex} + \underbrace{F_{rot}}_{Wing\ rotation} + \underbrace{F_{wc}}_{Wake\ capture} \tag{1.6}$$

$$F_{qs} = \underbrace{F_a}_{Added\ mass} + \underbrace{F_{trans}}_{LE\ vortex} + \underbrace{F_{rot}}_{Wing\ rotation} \tag{1.7}$$

The added mass (F_a) is a term used to account for the acceleration of the fluids around the wing. It accounts for force peaks at the beginning and end of the stroke and it can be determined by equation 1.8.

$$F_a = \rho\frac{\pi}{4}R^2\bar{c}^2(\ddot{\phi}\sin\alpha + \dot{\phi}\dot{\alpha}\cos\alpha)\int_0^1 \hat{r}\hat{c}^2(\hat{r})d\hat{r} - \ddot{\alpha}\rho\frac{\pi}{16}\bar{c}^3R\int_0^1 \hat{c}^2(\hat{r})d\hat{r} \tag{1.8}$$

Here, ρ is the density of air, R is the wing span of a single wing, $\bar{c}$ is the mean chord length, ϕ is the stroke angle, α is the angle of attack, $\hat{r}$ is the non dimensional span-wise position and $\bar{c}$ is the non dimensional chord-wise position.

The translational term (F_{trans}) accounts for the leading edge vortex. It is dependent on U_t (the wing tip velocity), $C_{Lt}(\alpha)$, and $C_{Dt}(\alpha)$. The latter two have been fitted empirically to equations 1.10 and 1.11, where S is the wing surface area and $\bar{r}_2^2$ is the non dimensional second moment of wing area [12].

$$\begin{aligned} F_{trans} &= \frac{\rho S U_t^2 \hat{r}_2^2(S)}{2}[C_{Lt}^2(\alpha) + C_{Dt}^2(\alpha)]^{1/2} && (1.9)\\ C_{Lt}(\alpha) &= 0.225 + 1.58\sin(2.13\alpha - 7.2) && (1.10)\\ C_{Dt}(\alpha) &= 1.92 - 1.55\cos(2.04\alpha - 9.82) && (1.11) \end{aligned}$$

The rotational component (F_{rot}) depends on $C_{rot,theo}$, a coefficient that can be determined from a formula derived from 2D Kutta-Jukowski theory, but also by using an empirically fitted formula that takes 3D effects into account. The coefficient depends on non-dimensional angular velocity (equation 1.12) and wing rotation axis, but equation 1.13 can be used as an approximation. F_{rot} is determined by equation 1.14.

$$\begin{aligned} \hat{\omega} &= \frac{|\dot{\phi}|\bar{c}}{U_t} && (1.12)\\ C_{rot,theo} &= \pi(0.75 - \hat{x}_0) && (1.13)\\ F_{rot,theo} &= C_{rot,theo}\cdot\rho U_t\dot{\alpha}\bar{c}^2R\int_0^1 \hat{r}\hat{c}^2(\hat{r})d\hat{r} && (1.14) \end{aligned}$$

The wake capture term (F_{wc}) is the unknown in the equation. The former three terms all depend on instantaneous velocity and acceleration, a property that suits quasi-steady modeling. The wake capture depends on the previous wing stroke and because of this no quasi-steady formulation can be given. This leaves us with a model that can provide a very reasonable estimate of the instantaneous forces on the wing during translation, and severely underestimates the forces during the start-up phase of a wing stroke (in both pronation and supination).

This quasi-steady theory decomposition shows the importance of wake capture in advanced, symmetric and delayed rotation [41]. It underestimates the drag force in the

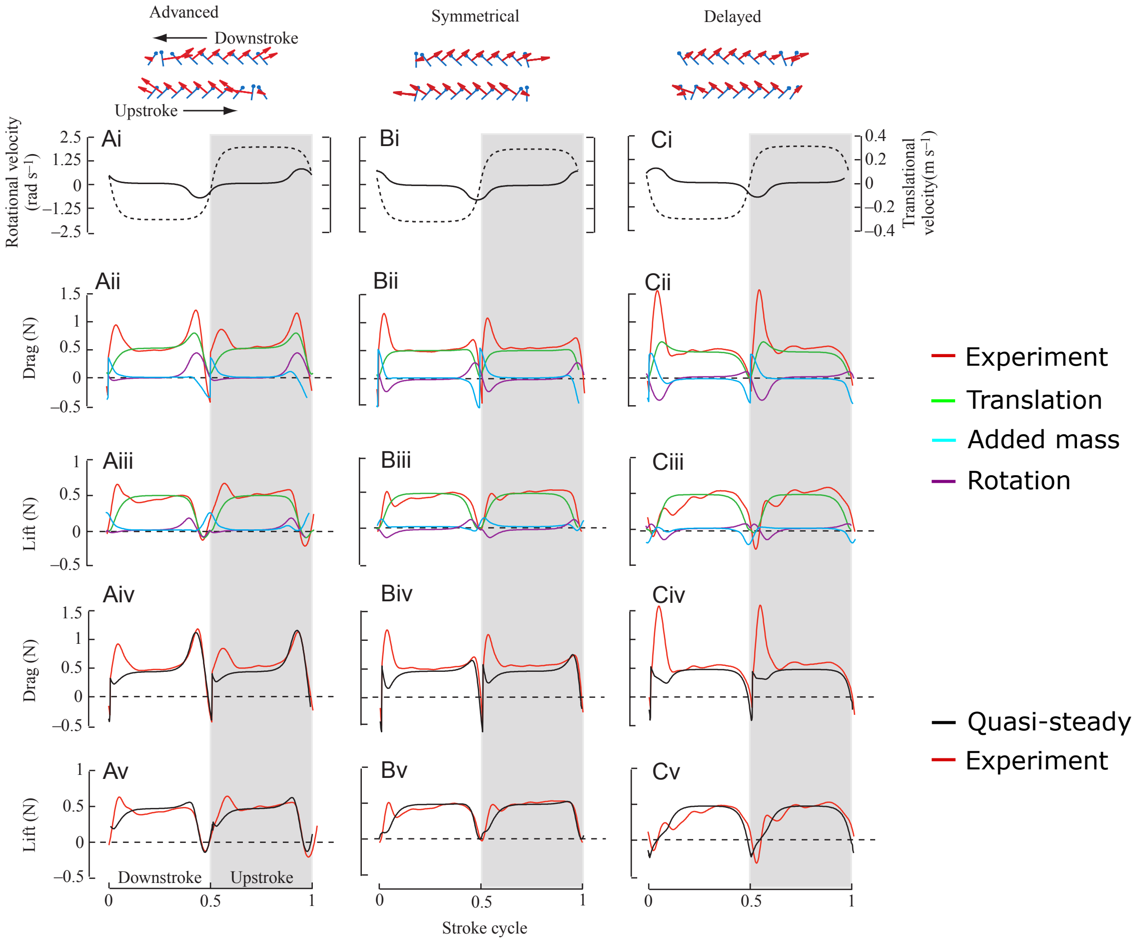

Figure 1.14: The aerodynamic forces on the wing measured experimentally and as computed from quasi-steady theory, figure adapted from [41].

experiment significantly in all cases, while the lift force shows better resemblance between quasi-steady and experimental results (figure 1.14).

The experiments with which the quasi-steady theory was validated were done at a Reynolds number of 112, but the authors remark that at higher Reynolds numbers (10^2 and 10^3) the measured forces are similar; "forces may not be crucially dependent on viscosity within the range of Reynolds number typical for most insects" [41]. The combination of theoretical decomposition and calibration by experiments makes it a reliable model for fruit flies, and it likely makes a decent estimate for the aerodynamic forces on hawk moth wings.

1.3 Hawk moth wing morphology

Because of its structure of veins and membrane it is feasible to model the structural mechanics of insect wings computationally. The membranes and veins are usually modeled by shells and beams, but in evaluating the performance of insect wings, it is important to keep in mind that the veins in the wing have multiple functions. Their primary function is to provide stiffness to the wing, but they also accommodate the mechanoreceptors and nerves, and supply the wings with fluids.

In general, insect wing veins receive their stiffness from a curticular outer surface. The inside of the vein often contains hemolymph (body fluid, analogous to blood), trachea (air pipes) and nerves [55]. Longitudinal veins are often the load bearing structure, while some species also have smaller cross veins to create a truss-structure. Figure 1.15 gives an overview of insect wing evolution.

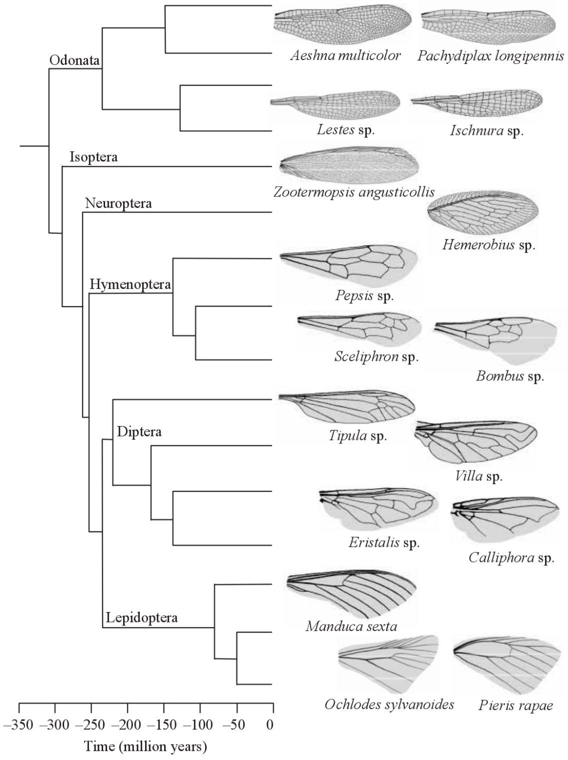

Figure 1.15: The evolution of wing venation across different insect species [7]

Wing stiffness

The hawk moth wing is characterized by a stiff leading edge and radial veins. The leading edge veins are most important in determining wing bending stiffness EI (figure 1.16). The eigenfrequency of insect wings have been found to be 4 times higher in the bending deformation mode and 10 times higher in the torsional deformation mode than the wing-beat frequency in dragonflies [26]. This natural frequency could play an important role in the aerodynamic phenomena that occur during pronation and supination. Flexible wings have been found to have superior lift properties compared to rigid wings [58].

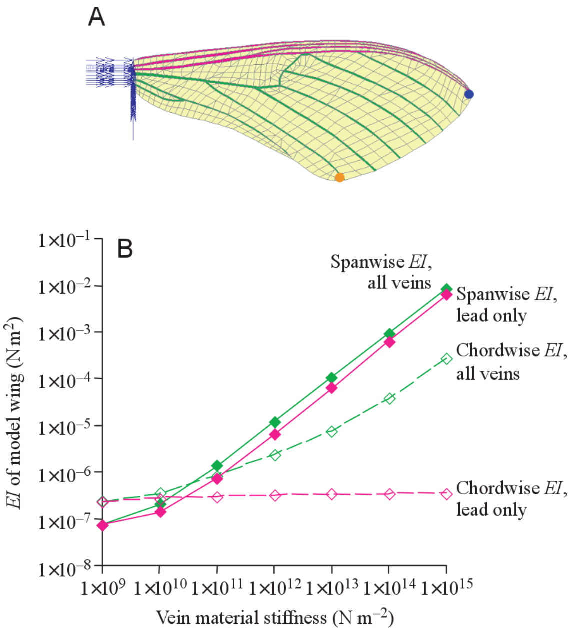

Figure 1.16: The impact of changing EI for lead vein or all veins on spanwise and chordwise EI [7]

.

The hawk moth wing has lower ratios of natural frequency to wing beat frequency than dragonflies [37]. Table 1.1 shows the natural frequency of the first four deformation modes. Note that the natural frequencies are of an order 2.4 to 3.4 higher than the wing-beat frequency of the hawk moth (25 Hz).

Table 1.1: The eigenfrequency of the hawk moth in air and vacuum for the first four deformation modes. Modal ratio (MR) are given in 95 % confidence intervals [37].

			In Air			In Vacuum		
Mode	Name	Description	Freq, Hz	MR	Damp, %	Freq, Hz	MR	Damp, %
1	Flap	1st Spanwise Bending	60	1.0	5.0	85	1.0	2.5
2	Feather	1st Spanwise Torsion	84	[1.39, 1.43]	5.0	105	[1.28, 1.32]	2.5
3	Saddle	1st Chordwise Bending	107	[1.80, 1.86]	5.0	138	[1.59, 1.65]	2.5
4	Bisaddle	2nd Chordwise Bending	142	[2.38, 2.48]	5.0	170	[2.16, 2.26]	2.5

Results from these structural simulations should be interpreted with care. Mechanical properties of biological materials are rarely homogeneous, wing excitation occurs in 3 axes of rotation, and the connection between the wing and the thorax is notoriously complicated. One of the difficulties in studying structural behavior of insect wings and halteres is that there is no obvious point at which the wing ends, or about which point it rotates. A large number of muscles have been identified in the thorax that are believed to play a role in the wing motion and how they work together is unknown.

Strain sensors on the wing

Campaniform sensilla are mechanoreceptors found in insects, reacting to local strain by sending action potentials to the nervous system. They can be easily be spotted, but their function is in many cases still unknown. At the base of the halteres, campaniform sensilla are used to detect strain caused by haltere deformation.

Campaniform sensilla consist of a dome-like structure with a nerve ending attached (figure 1.17). Electro-physiological experiments have formed the basis of the current understanding of how campaniforms respond to external strain. The campaniform sensilla in cockroach legs are positioned to detect strain along the leg axis, they rarely fire in strain other than from the principle direction. They also rarely fire under leg twist, and they are poor magnitude sensors [39, 59]. Furthermore, although campaniforms are believed function very similarly over a broad range of insect species, different types exit. Slow and fast campaniforms are found on the wings of blowflies, perhaps with the function to capture wing twist [10].

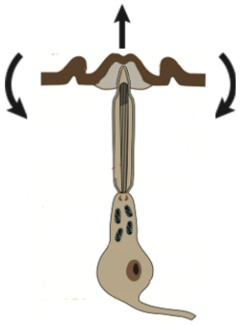

Figure 1.17: An overview of the campaniform sensilla structure, adapted from [27].

Recently it has been found that the spike-time precision of *Manduca sexta* campaniforms is comparable to those at the base of the haltere. Jitter is defined as the standard deviation of the spike arrival time, a small jitter will mean spikes arrive at a very predictable time, with little variability. This is required if the timing of the spikes is important. A single wing neuron was found to have a median jitter of 0.16 ms(∗), with a mean (‡)+- 1 standard deviation of 0.40 +- 0.70 ms. [9]. The jitter in the spike times of campaniform sensilla on the hawk moth fore wing can be seen in figure 1.18.

The interpretation of this precision is not straightforward. To get from this excitation to spikes in a neuron at the wing base, three unknown processes are involved. First, the stimulus causes a wing deformation. There is time delay associated with this, and stimulus history can play a role. It is thus unknown what the actual deformation was that caused the signal to trigger. Secondly, it is unknown where the mechanoreceptor belonging to this particular nerve is located, so even if we have a rough idea on what the wing deformation is at all locations, we are unsure which campaniform we are listening out of.

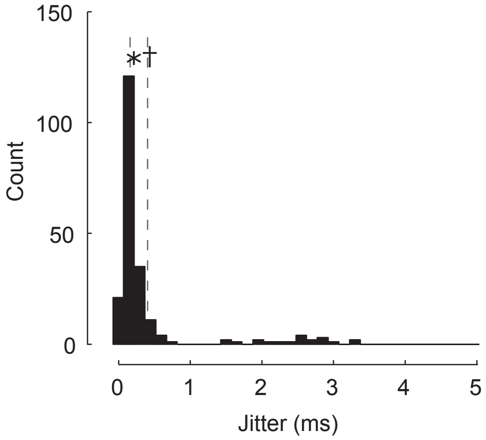

Figure 1.18: The spike arrival time of a single neuron of the hawk moth wing for 213 spiking events. The mean jitter is 0.16 ms($*$), the mean (‡)+- standard deviation is 0.40 +- 0.70 ms [9].

Thirdly, how deformation is transformed into a neural signal by the actual campaniform sensilla remains an open question.

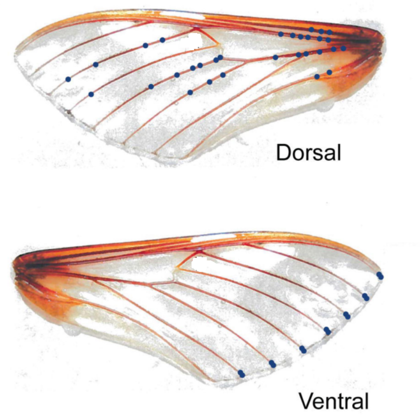

Figure 1.19: The distribution of campaniform sensilla on the wing of the hawk moth [9].

Wing sensor distribution

The fore wings of the *Manduca Sexta* have over 250 campaniform sensilla [9, 13]. In comparison, the haltere of the blowfly *Calliphora vicina* has 338 campaniform sensilla, its wings also counting 120-154 [20]. The sensilla on the *Manduca sexta* wings are mostly found dorsally of the forewing, conglomerating at the root of the wing, but they are also sparsely distributed over the veins at the first half of the chord 1.19. Ventrally, a number of Campaniform sensilla are located at the wing tip. The sensilla are never located on the membrane of the wing.

The idea of sensing wing twist has generated interest from an optimal sensor placement perspective. With a computational model the normal strain sensors at the base of the wing and shear strain sensors at the tip of the wing were found to work best in detecting wing twist (figure 1.20) [22].

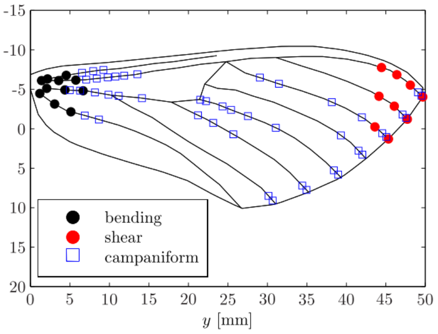

Figure 1.20: Optimal placement of strain sensors for detecting twist deformation along the wing [22].

Chapter 2

Methodology

Simulations and physical experiments will be used to determine the effect of inertial rotations on wing deformation. However, the simulations only take into account inertial forces. In section 2.1 an estimate of the inertial and aerodynamic forces is given to estimate the extend to which aerodynamic forces play a role in flapping wing deformation at hawk moth scale.

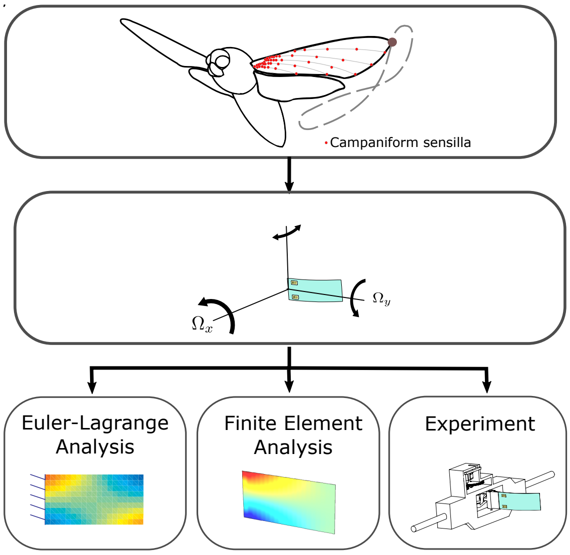

Figure 2.1: The wing of the hawk moth is approximated by a flat plate, and its wing motion is reduced to flapping around the $\bar{z}$ axis. An Euler-Lagrange simulation, a finite element simulation and experiments are used to simulate this simplified wing.

The simplified wing will be modeled with an Euler-Langrange derived system of differential equations, with a commercially available finite-element software, and with a physical model. The combination of results from these simulations and experiments is necessary because of the limitations and uncertainties each method brings. Figure 2.1 gives an overview of the simplifications made and the methods of simulation.

The wing model used in the simulations differs from the hawk moth wing in a few key aspects. Firstly, the membrane and venated wing structure are approximated by an acrylic flat plate. Secondly, the array of campaniform sensilla are modeled by two strain sensors at the left and right side of the wing base. Thirdly, the wing amplitude Φ will be 15^o, the elevation angle θ will be zero, and the wing will be rotated about an axis orthogonal to the wing root. Lastly, due to experimental constrains, the flapping frequency in the model is 10 Hz, instead of the 25 Hz that is observed in hawk moth flight.

As we will see in the following section, of the three inertial rotations the Ω_Z rotation does not result in any out of plane forces. Therefore the simulations and experiments will focus on the Ω_X and Ω_Y rotations only.

2.1 Theory

During flight, the hawk moth wing is subjected to inertial, gravitational and aerodynamic forces. Understanding the magnitude, direction, and dynamics of these forces will give an idea of the validity of the models.

$$\mathbf{F}_{total} = \mathbf{F}_{Inertial} + \mathbf{F}_{aerodynamic} + m\mathbf{g} \tag{2.1}$$

Inertial force estimate

To get an idea of the scale of the inertial components, we can take a look at a haltere with a mass equal to wing used in the models at a radial distance of half the wing length. The Centrifugal force will be underestimated in this way, since it depends quadratically on the radial distance to the center of rotation. The inertial forces can be determined by equation 8. The derivation of this equation can be found in appendix A.

$$\mathbf{F}_{Inertial} = \underbrace{m\frac{d^2\mathbf{r}}{dt^2}|_R}_{Linear\ acceleration} + \underbrace{m\frac{d\boldsymbol{\omega}}{dt} \times \mathbf{r}}_{Angular\ acceleration} + \underbrace{2m\boldsymbol{\omega} \times \frac{d\mathbf{r}}{dt}|_R}_{Coriolis\ force} + \underbrace{m\boldsymbol{\omega} \times (\boldsymbol{\omega} \times \mathbf{r})}_{Centrifugal\ force} \tag{2.2}$$

with: $\boldsymbol{\omega} = [\Omega_x, \Omega_y, \Omega_z]^T$ and $\mathbf{r} = [x, y, z]^T$

During constant rotation, the angular acceleration (also called Euler acceleration) is zero. To test the significance of angular accelerations all experiments will also be conducted with periodic rotations. In figure 2.2 the forces orthogonal to the stroke plane are shown for the three axes of rotation. The in-plane forces are much larger than the out of plane forces, but they do not result in wing twist.

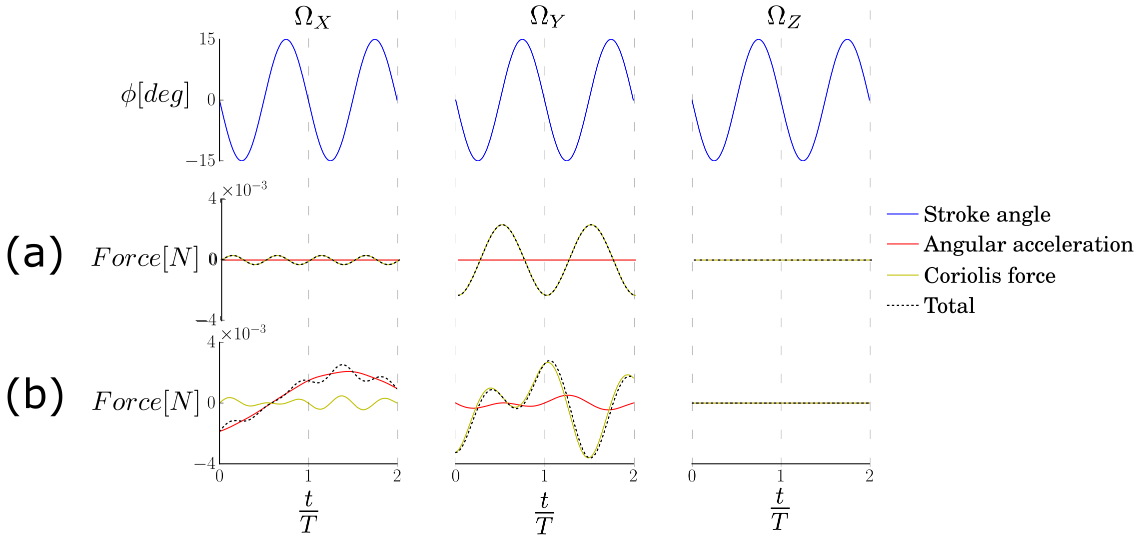

Figure 2.2: Forces acting on a point mass of $1.5 \cdot 10^{-4}$ kg, at r $= 2.5 \cdot 10^{-2}$m, flapping with an amplitude of $\phi = 15$ [deg] at 10 Hz, during (a) constant rotation of $\Omega = 6\pi[rads^{-1}]$, and (b) periodic rotation $\theta = 30 \cdot \sin(6\pi t)$.

Aerodynamic force estimate

Due to the unsteady phenomena there is still a lot of uncertainty in the aerodynamic theories for flapping flight. However, aerodynamic forces are small compared to inertial forces on the wings of the hawk moth during flight [8]. Furthermore, if we suppose that the principle of superposition is valid, the deflections of aerodynamic and inertial forces can be analyzed independently and added up later. This means that although the deflection due to aerodynamic forces might be larger than those due to the body rotation inertial terms, the inertial terms still can cause a detectable deformation.

$$F_{inst} = \underbrace{F_a}_{Added\ mass} + \underbrace{F_{trans}}_{LE\ vortex} + \underbrace{F_{rot}}_{Wing\ rotation} + \underbrace{\cancelto{0}{F_{wc}}}_{Wake\ capture} \tag{2.3}$$

$$F_{qs} = \underbrace{F_a}_{Added\ mass} + \underbrace{F_{trans}}_{LE\ vortex} + \underbrace{F_{rot}}_{Wing\ rotation} \tag{2.4}$$

The quasi-steady theory for flapping flight will be used to estimate the aerodynamic forces, it has been covered in detail in section 1.2. The angle of attack is determined by taking the arctangent of the wing tip velocity and the incoming velocity during a 3 rps inertial rotation around the x-axis. For simplicity, the wing is assumed to be rigid. The Reynolds number in the experiments is 10^3, slightly lower than that of the hawk moth.

The quasi-steady theory does not take into account wake capture, therefore we are left with aerodynamic forces due to added mass, wing rotation and wing translation, translation generally being dominant factor as it accounts for the leading edge vortex. All these forces act normal to the wing surface.

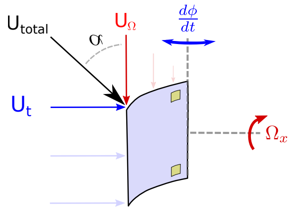

Figure 2.3: Angle of attack in the experiment, computed by the tangent between velocity from rotation and velocity from flapping.

$$C_{rot,theo} = \pi(0.75 - \hat{x}_0) \tag{2.5}$$

$$\alpha = \arctan(\frac{U_t}{U_\Omega}) \tag{2.6}$$

The angle of attach (α) is determined by taking the incoming velocity due to rotation and the incoming velocity due to flapping (figure 2.3 and equation 2.6). With a non dimensional angular velocity $\hat{\omega}$ of 0.4 and the wing longitudinal axis being the axis of rotation ($\hat{x}_0$=0.5), the rotation coefficient C_{rot_theo} was determined with equation 2.5 to be 0.785. A detailed description of the other parameters in equation 2.7,2.8 and 2.9 can be found in section 1.2.

$$F_a = \rho\frac{\pi}{4}R^2\bar{c}^2(\ddot{\phi}\sin\alpha + \dot{\phi}\dot{\alpha}\cos\alpha)\int_0^1 \hat{r}\hat{c}^2(\hat{r})d\hat{r} - \ddot{\alpha}\rho\frac{\pi}{16}\bar{c}^3R\int_0^1 \hat{c}^2(\hat{r})d\hat{r} \tag{2.7}$$

$$F_{trans} = \frac{\rho S U_t^2 \hat{r}_2^2(S)}{2}[C_{Lt}^2(\alpha) + C_{Dt}^2(\alpha)]^{1/2} \tag{2.8}$$

$$F_{rot} = C_{rot,theo}\cdot\rho U_t\dot{\alpha}\bar{c}^2R\int_0^1 \hat{r}\hat{c}^2(\hat{r})d\hat{r} \tag{2.9}$$

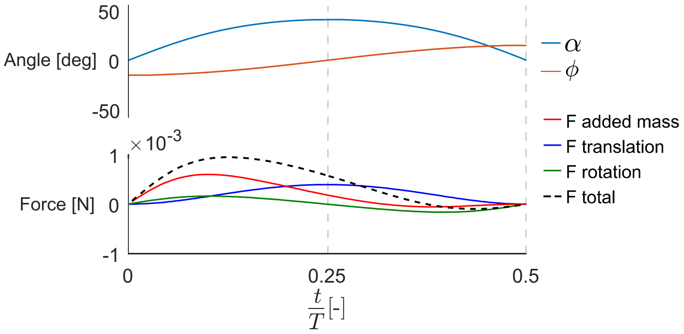

Figure 2.4: Aerodynamic forces on a flat plate with $\phi = 15[^o]$, $f_f = 10[Hz]$ and $\Omega_X = 6\pi[rads^{-1}]$, computed with equation 2.4.

The aerodynamic forces (figure 2.4) are of the same order as the out of plane gyroscopic forces, both are in the order of 10^{-3} Newton. These aerodynamic forces act in the stroke plane, but unlike the inertial forces that cause bending, the aerodynamic forces are not evenly distributed chord-wise. Therefore aerodynamic forces are likely to cause some form of wing twist.

Gravity

Although gravity is present on the moth wings, it will be only a fraction of the aerodynamic force. A moth wing makes up about 4 to 7 % [54] of the body weight in hawk moths. Furthermore, in our analysis the direction of the gravity vector is not specified. It is not modeled in the computational simulations, but it can play a role in the experiments. The gravitational force acting on the wing equals $1.47 \cdot 10^{-3}$, which is in the same order of magnitude as the other forces.

2.2 Model description

The wing is made from a sheet of acrylic plastic with dimensions of 50 x 20 x 0.127 mm. In the simulations, the two probes are located symmetrically around the longitudinal axis, at 5 mm and 2 mm from the wing root and edges respectively (figure 2.5). In the experimental setup these wing dimensions and strain probe locations are approximated.

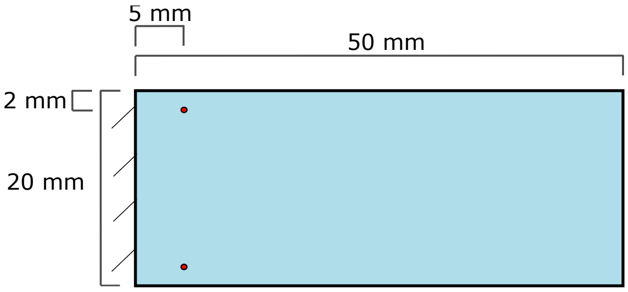

Figure 2.5: Wing dimensions and locations of the wing probes.

Table 2.1: Table of wing parameters.

Parameter	value	unit
L	50	mm
W	20	mm
T	0.127	mm
ρ	1180	$\frac{kg}{m^3}$
m	$1.50 \cdot 10^{-5}$	kg
E	$3 \cdot 10^9$	$\frac{N}{m^2}$

Wing excitation

The wing is subjected to sinusoidal excitation with a stroke amplitude (Φ) of 15 degrees at a flapping frequency (f_f) of 10 Hz. The excitation in the experiments is only an approximation to this because of two reasons. Firstly, the 4-bar mechanism to convert motor rotation into oscillation induces higher order harmonics. These are especially noticeable at larger amplitudes. Secondly, the wing is clamped not at the center of rotation, but instead it has a radial offset of 10 mm.

To determine the effect of both angular velocity and angular accelerations, one set of experiments was done with a constant angular velocity, while the second set constitutes of experiments with periodic motion with amplitude ($\Theta_{Periodic}$). The rotation frequency (f_r) was either 0 or 3. An overview of the experimental parameters is given in table 2.2.

$$\theta_{Constant} = 2\pi f_r \cdot t + C \tag{2.10}$$

$$\Omega_{Constant} = 2\pi f_r \tag{2.11}$$

$$\theta_{Periodic} = \Theta_{Periodic} \cdot \sin(2\pi f_r t) \tag{2.12}$$

$$\Omega_{Periodic} = \Theta_{Periodic} \cdot 2\pi f_r \sin(2\pi f_r t) \tag{2.13}$$

Table 2.2: Wing excitation parameters.

Parameter	value	unit
f_f	10	Hz
Φ	15	degrees
$\Theta_{Periodic}$	30	degrees
f_r	0,3	Hz

Chapter 3

Computational models

Two computational models were used to simulate the flapping wing. The first model is an Euler-Lagrange derived set of differential equations, solved with MATLAB [33]. The second is an implementation of the flapping wing in the commercially avaiable Finite-element software COMSOL [35].

3.1 Analytic Euler-Lagrange model

The Euler-Langrange equation can be used to find the local minima of a differentiable function, minimizing the difference between the change in kinetic and change in potential energy. A damping term $\frac{\partial D}{\partial \dot{q}_i}$ is added to stabilize the model. The derivation of equation 3.1 can be found in appendix B.

$$\frac{d}{dt}(\frac{\partial(T)}{\partial \dot{q}_i}) - \frac{\partial(T)}{\partial q_i} + \frac{\partial(V)}{\partial q_i} + \frac{\partial D}{\partial \dot{q}_i} = Q_i \tag{3.1}$$

The flat plate Euler-Lagrange model was initially developed for constant and periodic rotation about the axis orthogonal to the wing stroke plane of a flat plate [16]. For the purpose of this research, it was adapted to simulate rotation around all three axis of rotation. The model is a single flat plate with nodes at each corner. The two nodes at the base (1 and 2) are constrained and will experience a pre-described oscillation:

$$\phi_1 = \phi_2 = \Phi sin(2\pi f_f t) \tag{3.2}$$

Here Φ is equal to 15 [deg] and f_f of 10 [Hz]. The nodes 3 and 4 at the tip each have 3 degrees of freedom. Figure 3.1 shows the orientation and nodes of the wing in the model:

$$[\delta_3, \phi_3, \theta_3, \delta_4, \phi_4, \theta_4]^T \tag{3.3}$$

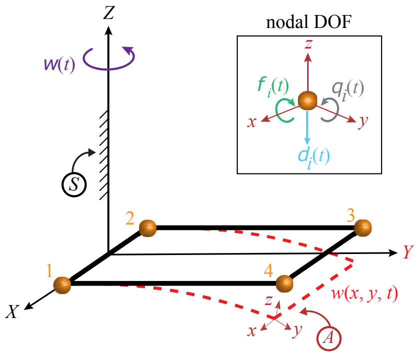

Figure 3.1: Reference frame describing nodes and degrees of freedom in the Euler-Lagrange model [16].

The nodes are fixed in x and y, they do not stretch. They can only deform in z (δ), rotate around x (ϕ) and rotate around y (θ).

Shape functions

For each of the two wing tip nodes, three shape functions are available:

$$\bar{N}_i(x,y) = \begin{bmatrix} \frac{1}{8}(1+\xi_0)(1+\eta_0)(2+\xi_0+\eta_0-\xi^2-\eta^2) \\ \frac{a}{8}\xi_i(1-\xi_0)^2(\xi_0-1)(\eta_0+1) \\ \frac{b}{8}\eta_i(1+\eta_0)^2(1+\xi_0)(\eta_0-1) \end{bmatrix} \tag{3.4}$$

They meet the requirement of being largest at their corresponding node and zero at the other nodes. The shape functions are defined with non-dimensional coefficients:

$$\xi = \frac{x - x_c}{a} \tag{3.5}$$

$$\xi_i = \frac{x_i - x_c}{a} \tag{3.6}$$

$$\xi_0 = \xi\xi_i \tag{3.7}$$

$$\eta = \frac{y - y_c}{b} \tag{3.8}$$

$$\eta_i = \frac{y_i - y_c}{b} \tag{3.9}$$

$$\eta_0 = \eta\eta_i \tag{3.10}$$

The coefficients are formulated with a being the half-chord length and b the half-span length. The center of the plate (x_c, y_c) is at (0,b). The i subscript (x_i, y_i) denotes the location of the i^{th} node.

Since we have two free nodes, the deformation of the plate are mapped on six shape functions. Deformation value w is then the sum of the shape functions and their corresponding value q_i. The derivatives of these are provided here:

$$\dot{w} = \sum N_i \dot{q}_i \tag{3.11}$$

$$\frac{\partial \dot{w}}{\partial q_i} = 0 \tag{3.12}$$

$$\frac{\partial \dot{w}}{\partial \dot{q}_i} = \sum N_i \tag{3.13}$$

$$\omega = \sum N_i q_i \tag{3.14}$$

$$\frac{\partial w}{\partial q_i} = \sum N_i \tag{3.15}$$

$$\frac{\partial w}{\partial \dot{q}_i} = 0 \tag{3.16}$$

Derivation equations of motion

The potential and kinetic energy now need to be defined in our coordinate system.

$$T = \frac{1}{2}\int\int \rho h \bar{v} \cdot \bar{v} dxdy \tag{3.17}$$

$$V = \frac{h^3}{24}\int^{2b}\int_{-a}^{a} [\bar{\chi}(x,y,t)^T \bar{D}[\bar{\chi}(x,y,t)]dxdy \tag{3.18}$$

where χ are the principal stress components. The other parameters that we need to define are velocity $\bar{v}$, rotation $\bar{\omega}$ and position $\bar{r}$. Translational velocity of the frame of origin $\bar{v_0}$ is provided for completeness, it is zero for our purposes.

$$\bar{v_0} = [u, v, w]^T = [0, 0, 0]^T \tag{3.19}$$

$$\bar{\omega} = [P, Q, R]^T = [\frac{d\phi}{dt}, 0, \Omega_x]^T \tag{3.20}$$

$$\bar{r} = [x, y, w(x, y, t)]^T \tag{3.21}$$

$$\frac{d\bar{r}}{dt} = [0, 0, \dot{w}]^T \tag{3.22}$$

In the definition of our plate, in the position vector $\bar{r}$, only the position in z depends on time. Expanding the velocity, the following is obtained:

$$\bar{v} = \bar{v_0} + \frac{d}{dt}\bar{r} + \bar{\omega} \times \bar{r} = \frac{d}{dt}\bar{r} + \bar{r} \times \bar{\omega} \tag{3.23}$$

$$\bar{\omega} \times \bar{r} = \begin{bmatrix} i & j & k \\ P & Q & R \\ x & y & w \end{bmatrix} = \begin{bmatrix} i(Qw - Ry) \\ j(Rx - Pw) \\ k(Py - Qx) \end{bmatrix} \tag{3.24}$$

$$\bar{v} = \begin{bmatrix} i(Qw - Ry) \\ j(Rx - Pw) \\ \dot{w} + (Py - Qx) \end{bmatrix} \tag{3.25}$$

Expanding the velocity squared:

$$\begin{aligned}
\bar{v}\cdot\bar{v} &= (Qw-Ry)^2+(Rx-Pw)^2+(\dot{w}+Py-Qx)^2 && (3.26)\\
(Qw-Ry)^2 &= Q^2w^2-2QRyw+R^2y^2 && (3.27)\\
(Rx-Pw)^2 &= P^2w^2-2PRxw+R^2x^2 && (3.28)\\
(\dot{w}+Py-Qx)^2 &= \dot{w}^2+2\dot{\omega}Py-2\dot{\omega}Qx-2PQxy+P^2y^2+Q^2x^2 && (3.29)
\end{aligned}$$

First the kinetic energy dependence on $\dot{q}_i$ in Lagrange's equation 3.1 is considered. Since the derivative w.r.t. $\dot{q}_i$ is taken, anything without $\dot{\omega}$ is zero:

$$\begin{aligned}
\frac{d}{dt}(\frac{\partial(T)}{\partial\dot{q}_i}) &= \frac{d}{dt}\frac{1}{2}\int\int\rho h(\frac{\partial(\bar{v}\cdot\bar{v})}{\partial\dot{q}_i})dxdy && (3.30)\\
\frac{d}{dt}(\frac{\partial(T)}{\partial\dot{q}_i}) &= \frac{1}{2}\int\int\rho h\frac{d}{dt}(\frac{\partial(\dot{w}^2+2\dot{\omega}Py-2\dot{\omega}Qx)}{\partial\dot{q}_i})dxdy && (3.31)\\
\frac{d}{dt}(\frac{\partial(T)}{\partial\dot{q}_i}) &= \frac{1}{2}\int\int\rho h\frac{d}{dt}(\sum N_i(2\sum_i\dot{q}_i+2Py-2Qx))dxdy && (3.32)
\end{aligned}$$

We now split into a term depending on $\ddot{q}$, and terms only depending on body rotation $\bar{\omega}$, in the form of $\dot{P}$ and $\dot{Q}$.

$$\begin{aligned}
\frac{d}{dt}(\frac{\partial(T)}{\partial\dot{q}_i}) &= \int\int\rho h\sum N_i\sum_i N_i\ddot{q}_i)dxdy+\int\int\rho h\sum N_i(\dot{P}y-\dot{Q}x)dxdy && (3.33)\\
\frac{d}{dt}(\frac{\partial(T)}{\partial\dot{q}_i}) &= M\ddot{q}_i+M_a\begin{bmatrix}0\\-\dot{Q}\\\dot{P}\end{bmatrix} && (3.34)
\end{aligned}$$

with:

$$\begin{aligned}
M &= \int\int\rho h\sum N_i\sum_i N_i dxdy && (3.35)\\
M_a &= \left[\int\int\rho h\sum(N_i)\,dxdy \quad \int\int\rho h\sum(N_ix)\,dxdy \quad \int\int\rho h\sum(N_iy)\,dxdy\right] && (3.36)
\end{aligned}$$

Now we expand the second term of Lagrange's equation:

$$\begin{aligned}
-\frac{\partial(T)}{\partial q_i} &= -\frac{1}{2}\int\int\rho h(\frac{\partial(\bar{v}\cdot\bar{v})}{\partial q_i}) && (3.37)\\
-\frac{\partial(T)}{\partial q_i} &= -\frac{1}{2}\int\int\rho h(\frac{\partial((P^2+Q^2)w^2-2w(PRx+QRy))}{\partial q_i})dxdy && (3.38)
\end{aligned}$$

Anything without ω can be discarded:

$$-\frac{\partial(T)}{\partial q_i} = -\frac{1}{2}\int\int \rho h \sum N_i \left(2(P^2+Q^2)\sum N_i q_i - 2(PRx+QRy)\right) dxdy \tag{3.39}$$

$$-\frac{\partial(T)}{\partial q_i} = -\int\int \rho h \sum N_i \left((P^2+Q^2)\sum N_i q_i\right) dxdy + \int\int \rho h \sum N_i \left((PRx+QRy)\right) dxdy \tag{3.40}$$

The equation can be split into Centrifugal and Coriolis force, the former being:

$$F_{centrifugal} = -(P^2+Q^2)\int\int \rho h \sum N_i \cdot \sum N_i q_i dxdy \tag{3.41}$$

$$F_{centrifugal} = -(P^2+Q^2) M q_i \tag{3.42}$$

$$\tag{3.43}$$

The Coriolis force consists of the following:

$$F_{Coriolis} = \int\int \rho h (PR\sum N_i x + QR\sum N_i y) dxdy \tag{3.44}$$

$$F_{Coriolis} = Ma \begin{bmatrix} 0 \\ PR \\ QR \end{bmatrix} \tag{3.45}$$

Together they make:

$$-\frac{\partial(T)}{\partial q_i} = -(P^2+Q^2) M q_i + Ma \begin{bmatrix} 0 \\ PR \\ QR \end{bmatrix} \tag{3.46}$$

The third term in Lagrange's equation will depend on the potential energy stored in the structure of the wing. This is defined as the strain integrated over the plate.

$$V = \frac{h^3}{24}\int^{2b}\int_{-a}^{a} [\bar{\chi}(x,y,t)^T \bar{D}[\bar{\chi}(x,y,t)] dxdy \tag{3.47}$$

$$\bar{\chi}(x,y,t) = \left[\frac{\partial^2 w}{\partial x^2}\frac{\partial^2 w}{\partial y^2}\frac{\partial^2 w}{\partial xy}\right]^T \tag{3.48}$$

$$D = \frac{E}{(1-v^2)}\begin{bmatrix} 1 & v & 0 \\ v & 1 & 0 \\ 0 & 0 & (1-v) \end{bmatrix} \tag{3.49}$$

Here the deformation $w(x,y,t)$ also depends on the shape functions. Now we take the derivative w.r.t q_i:

$$\frac{\partial(V)}{\partial q_i} = \frac{h^3}{12}\int^{2b}\int_{-a}^{a} [\left[\frac{\partial^2 N_i}{\partial x^2}\frac{\partial^2 N_i}{\partial y^2}\frac{\partial^2 N_i}{\partial xy}\right]^T \bar{D} [\left[\frac{\partial^2 N_i}{\partial x^2}\frac{\partial^2 N_i}{\partial y^2}\frac{\partial^2 N_i}{\partial xy}\right] q_i dxdy \tag{3.50}$$

$$\frac{\partial(V)}{\partial q_i} = Kq_i \tag{3.51}$$

With:

$$K = \frac{h^3}{12}\int^{2b}\int_{-a}^{a} [\left[\frac{\partial^2 N_i}{\partial x^2}\frac{\partial^2 N_i}{\partial y^2}\frac{\partial^2 N_i}{\partial xy}\right]^T \bar{D} [\left[\frac{\partial^2 N_i}{\partial x^2}\frac{\partial^2 N_i}{\partial y^2}\frac{\partial^2 N_i}{\partial xy}\right] \tag{3.52}$$

Damping

A mass proportional damping is used, it is an extra 4th term in the equation.

$$F_{Damp} = -\eta M\dot{q} \tag{3.53}$$

with $\eta = 0.66$ a value found on moth wing experiments [16].

Putting things together

We can now fill in the terms in the Euler lagrange equation:

$$\frac{d}{dt}(\frac{\partial(T)}{\partial \dot{q}_i}) - \frac{\partial(T)}{\partial q_i} + \frac{\partial(V)}{\partial q_i} + \frac{\partial D}{\partial \dot{q}_i} = Q_i \tag{3.54}$$

Equilibrium is maintained with no external forces added ($Q_i = 0$):

$$M\ddot{q}_i + M_a\begin{bmatrix}0\\-\dot{Q}\\\dot{P}\end{bmatrix} - (P^2+Q^2)Mq_i + M_a\begin{bmatrix}0\\PR\\QR\end{bmatrix} + Kq_i - \eta M\dot{q} = 0 \tag{3.55}$$

This can be restructure to have only a $\ddot{q}_i$ left hand side:

$$M\ddot{q}_i = -M_a\begin{bmatrix}0\\-\dot{Q}\\\dot{P}\end{bmatrix} + (P^2+Q^2)Mq_i - M_a\begin{bmatrix}0\\PR\\QR\end{bmatrix} - Kq_i + \eta M\dot{q} \tag{3.56}$$

$$\ddot{q}_i = M^{-1}\left(-M_a\begin{bmatrix}0\\-\dot{Q}\\\dot{P}\end{bmatrix} + (P^2+Q^2)Mq_i - M_a\begin{bmatrix}0\\PR\\QR\end{bmatrix} - Kq_i + \eta M\dot{q}\right) \tag{3.57}$$

This can now be turned into a system of equations:

$$\begin{bmatrix}\dot{q}\\\ddot{q}\end{bmatrix} = \begin{bmatrix}0 & 1\\(P^2+Q^2-M^{-1}K) & \eta\end{bmatrix}\begin{bmatrix}q\\\dot{q}\end{bmatrix} - \begin{bmatrix}0\\M^{-1}M_a\begin{bmatrix}0\\\dot{Q}-PR\\-\dot{P}-QR\end{bmatrix}\end{bmatrix} \tag{3.58}$$

This is solved with MATLAB [33] with a fourth order Rutta-Kunge scheme.

Extracting position and strain

From the solution to the system of equations the strain can be extracted:

$$\epsilon_y = \sum \frac{\partial^2 N_i}{\partial y^2} q_i \cdot -\frac{h}{2} \tag{3.59}$$

3.2 Finite element model

The wing is implemented as a flat plate with a mesh of 50 by 10 by 3 elements along its length, width and thickness respectively. The wing is connected to a rod, mounted in a gimbal frame of three concentric rings, where the outer ring is fixed in space. Different boundary conditions can be subscribed by applying rotating condition on the connection points between the rings.

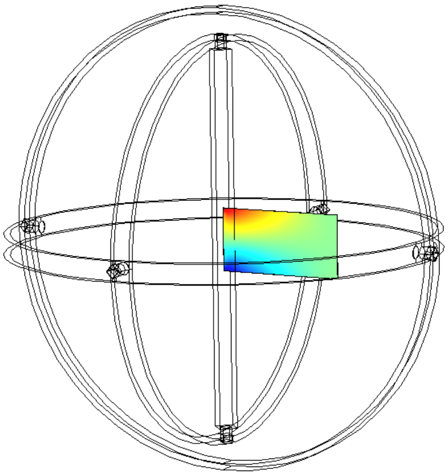

Figure 3.2: The implementation of the comsol wing model. The wing is fixated on a rod, mounted in a gimbal of three concentric rings.

Stability is achieved by applying a ramp function to flapping motion and the inertial rotation. This ramp function starts at $t/T = 2$, and lasts one flapcycle. Second order smoothing is applied at the start and the end of the ramp. The effect of mesh size was tested by changing the mesh from very course to very fine. Refining the mesh beyond (50x10x3) lead to an increased magnitude in the strain at the probe points, however, more refined meshes did not alter the shape of the stress curve. Figure 3.3 shows the difference in strain between the left and the right wing strain probe, as described in section 2.2. Table 3.1 gives an overview of the run times. Although the frequency of the stress is likely to be accurate, the magnitude is uncertain because it does not converge with increasing mesh size.

Table 3.1: Run times of different mesh sizes for one second simulations (10 flapcycles) with $\phi = 15[^o]$, $f_f = 10[Hz]$, and $\Omega_x = 6\pi[rads^{-1}]$ on a HP ZBook with a i7-4500U processor and 8 GB RAM.

Mesh #	Elements in LxWxH	Runtime [s]
1	20x8x4	446
2	30x8x6	894
3	50x10x3	733
4	60x15x8	4066

A relative tolerance of 10^{-6} was used. A narrower tolerance did not change the results, nor did it change the results of the mesh convergence study.

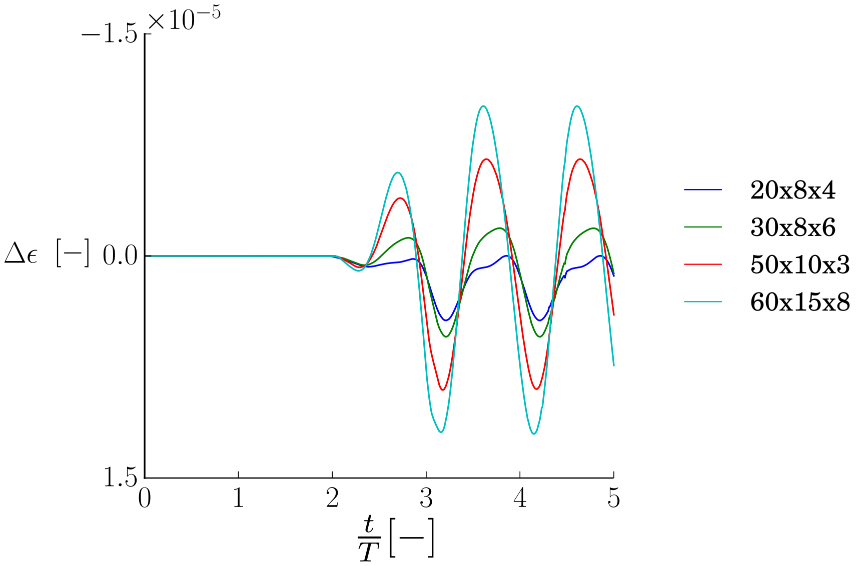

Figure 3.3: Difference in strain between the left and the right strain probe of the model wing for different meshes.

Chapter 4

Experimental setup

For the purpose of these experiments, a flapping wing device was designed and built. This device flaps with the same parameters as the computational simulations ($f_f = 10Hz$, $\Phi = 15^o$). The battery powered motor and data acquisition system (DAQ) ensured a standalone system, capable of continuous rotation. Two wing mounted strain gauges directly connect to the DAQ, consisting of a wheatstone bridge, an amplifier and an A/D converter. Steel rods protrude out on either side of the device, these rods are used to mount the device on one of two rotation rigs, for either Ω_X or Ω_Y rotations. Figure 4.1 shows a sketch of the flapping wing device.

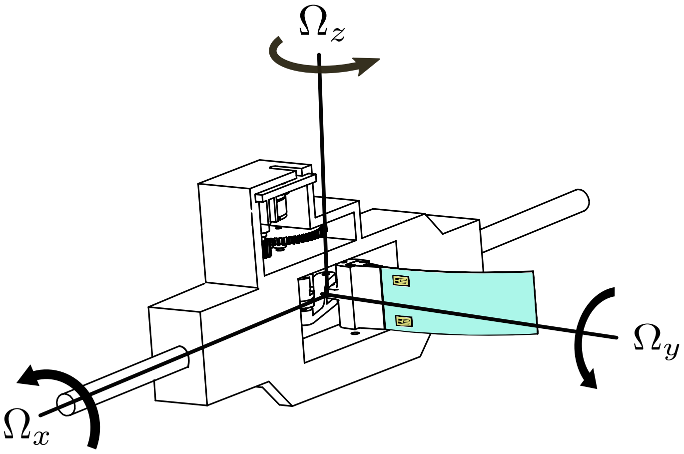

Figure 4.1: Sketch of the flapping wing device. The three rotations ($\Omega_X, \Omega_Y, \Omega_Z$) are drawn for reference.

4.1 Experiment design

A brushless motor, controlled with an electronic speed controller (ESC) and an RPM counter, drives the gear box. At $1/6^{th}$ the motor speed, the gearbox drives the 4-bar mechanism to turn rotation into periodic translation. The translation is delivered to a beam with the wing mounted on the other side of the hinge.

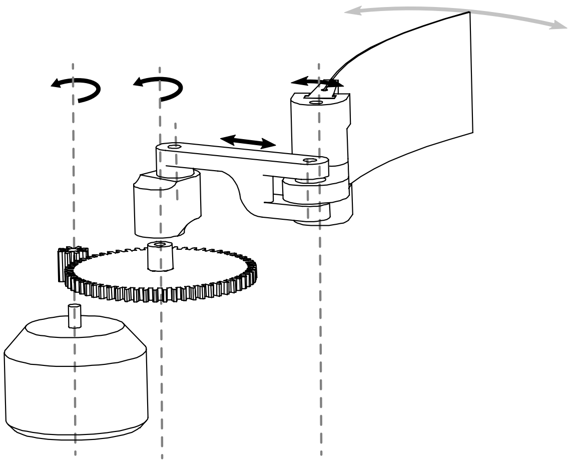

Figure 4.2: Sketch of the flapping wing mechanism.

The inertial rotations are realized by mounting the flapping wing device in a larger frame. For rotations in Ω_X, one end of the rod of the device is directly connected to a stepper motor, the other end is constrained by a bearing (figure 4.3 (a)). Rotations in Ω_Y are realized by fixating the rod on a frame, where now the entire frame rotates (figure 4.3 (b).

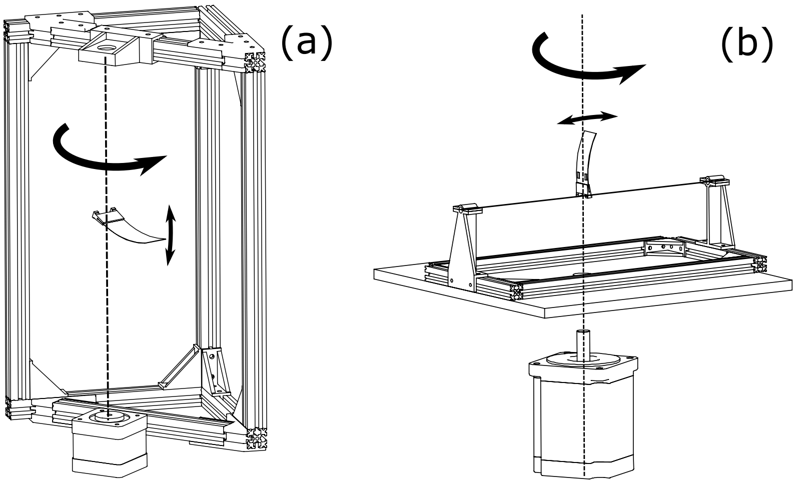

Figure 4.3: Sketch of the two rotation devices. (a) The rotation device for Ω_X rotations. (b) The rotation device for Ω_Y rotations.

Data acquisition system design

The two 350 Ω 3mm OMEGA Engineering strain gauges have 15 cm leads that connect to either one half wheatstone bridge or two quarter wheatstone bridges. The bridge signal is amplified by 1000 (ANALOG DEVICES AMP04) and connected to an analog ARDUINO UNO pin. The A/D chip of the Arduino reads the pin with an approximately one kilohertz sampling rate (SR). This is then logged onto an SD card with an ADAFRUIT SD-shield. The wheatstone bridges and their amplifiers live on a custom designed shield that stacks on top of the SD-shield. A detailed Printed Circuit Board (PCB) design can be found in the digital supplement (see appendix C). Figure 4.4 gives an overview of the steps from strain to the recorded numerical value.

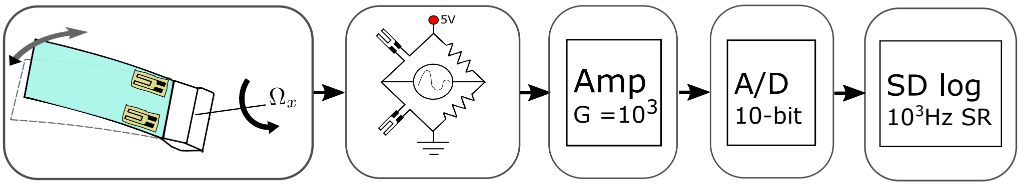

Figure 4.4: Overview of the data acquisition system.

Overview of setup

Figure 4.5 shows the flapping wing experiment setup.

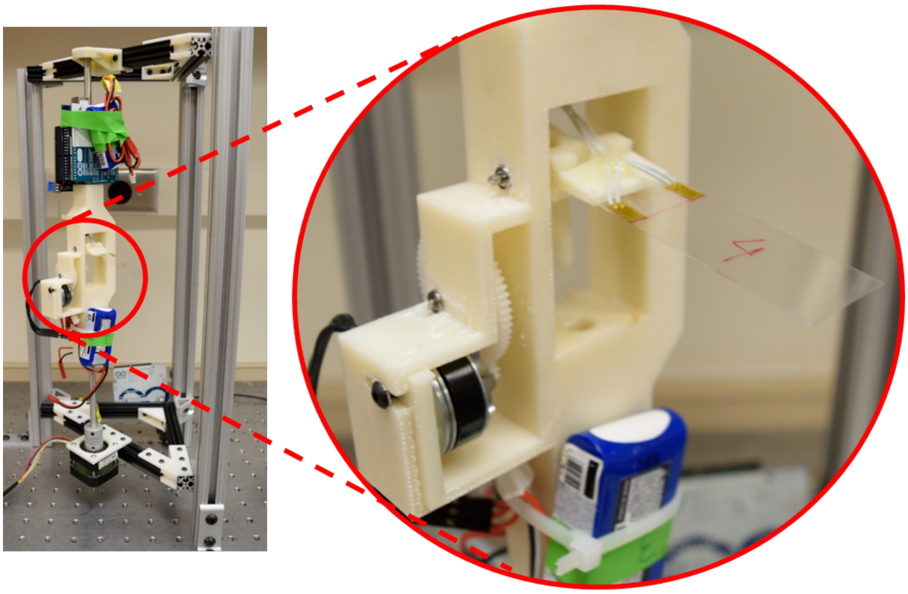

Figure 4.5: Picture and detailed picture of the flapping wing setup for rotations in Ω_X.

4.2 Calibration

The data recorded on the SD-card consist of a microsecond time stamp and a 10-bit numerical value for each recorded channel. In case of a quarter bridge configuration, this 10-bit value needs to be converted back to the strain value. However, if the half wheatstone bridge is used, the numerical value recorded represents the difference strain between the two gauges.

In the case of two quarter bridge configurations, the difference in strain between the two strain gauges will be determined during post-processing. The advantage of this method comes from the fact that the signal is easier to calibrate and interpret. The half bridge configuration has the advantage that by taking the difference before the amplification and digitization, the large common bending mode is mostly filtered out. This yields a cleaner signal, although interpretation and calibration require care.

Resistance based strain gauge

This section will go over the conversion from the numerical value to strain on the wing. Strain causes a change in resistance of the strain gauges according to equation 4.3.

$$K = \frac{\frac{\Delta R}{R}}{\epsilon} \tag{4.1}$$

$$\Delta R = R \cdot K \cdot \epsilon \tag{4.2}$$

$$R_G = R + \Delta R = R + R \cdot K \cdot \epsilon \tag{4.3}$$

Here K is the gauge factor, ϵ is strain and $R_G(\epsilon)$ is the resistance of the gauge under the strain ϵ.

Wheatstone bridge

To convert a difference in resistance into a difference in voltage a wheatstone bridge is used (figure 4.6).

A difference in resistance of a combination of the resistors in the bridge causes a voltage differential between the left and the right side of the bridge. This bridge voltage (V_G) can be calculated by equation 4.4, where V_{ex} is the excitation voltage (5 Volt in the case of the experiment).

$$V_G = \left(\frac{R_2}{R_1 + R_2} - \frac{R_3}{R_3 + R_4} \right) \cdot V_{ex} \tag{4.4}$$

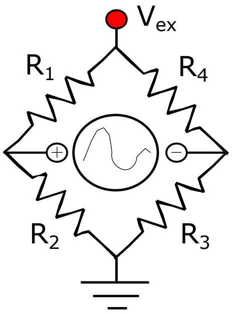

Figure 4.6: Schematic of a wheatstone bridge. If one of the resistors varies (e.g. it is a strain gauge), it is called a quarter bridge configuration. In case two gauges in series vary, it is called a half bridge configuration.

From bridge voltage to numerical value

The bridge voltage V_G is fed into the amplifier with 10^3 gain and with a reference of 2.5 Volt. Subsequently, this A_{in} is read by a 10-bit Analog-to-Digital converter (A/D) that reads voltages from 0 to 5 to a numerical value (NV) between 0 and 1023. With an excitation voltage of 5V, a 10-bit analog to digital converter has a resolution of $49mV$.

$$A_{in} = 10^3 \cdot V_G + 2.5 \tag{4.5}$$

$$NV = A_{in} \frac{1023}{5} \tag{4.6}$$

$$V_G = \frac{NV \frac{5}{1023} - 2.5}{10^3} \tag{4.7}$$

Quarter wheatstone bridge

The quarter Wheatstone bridge configuration (figure 4.7) takes the change in resistance (ΔR) of a single strain gauge, and converts this into a voltage according to equation 4.10.

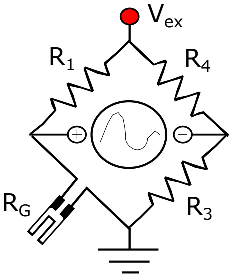

Figure 4.7: A quarter wheatstone configuration. One of the four resistors is variable in resistance, changing the bridge potential difference as a result.

The potential that results from a difference in strain by R_G is calculated by equation 4.10, where all the resistors have the same value, (in case of the experiments $R = 350\Omega$).

$$V_G = \left(\frac{R_G}{R_1 + R_G} - \frac{R_3}{R_3 + R_4} \right) \cdot V_{ex} \tag{4.8}$$

$$V_G = 5 \left(\frac{R + R \cdot K \cdot \epsilon}{R + R + R \cdot K \cdot \epsilon} - 0.5 \right) \tag{4.9}$$

$$V_G = 5 \left(\frac{1 + \cdot K \cdot \epsilon}{2 + K \cdot \epsilon} - 0.5 \right) \tag{4.10}$$

$$\epsilon = \frac{\frac{2}{5} V_G}{\frac{K}{2} - \frac{V_G}{5}} \tag{4.11}$$

Half Wheatstone bridge

The half Wheatstone bridge configuration (figure 4.8) two strain gauges change in resistance.

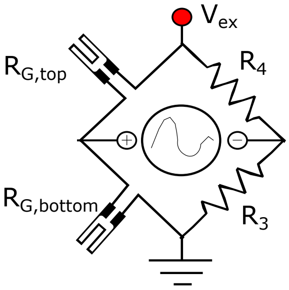

Figure 4.8: The half Wheatstone bridge configuration. Two strain gauges in series change the bridge potential.

The bridge voltage of the half Wheatstone bridge can be calculated with equation 4.16.

$$V_G = \left(\frac{R_{G,bottom}}{R_{G,top} + R_{G,bottom}} - \frac{R_3}{R_3 + R_4} \right) \cdot V_{ex} \tag{4.12}$$

$$V_G = 5 \left(\frac{R + R \cdot K \cdot \epsilon_{bottom}}{R + R \cdot K \cdot \epsilon_{bottom} + R + R \cdot K \cdot \epsilon_{top}} - 0.5 \right) \tag{4.13}$$

$$V_G = 5 \left(\frac{1 + K \cdot \epsilon_{bottom}}{2 + K \cdot (\epsilon_{bottom} + \cdot \epsilon_{top})} - 0.5 \right) \tag{4.14}$$

In the ideal situation, wing bending results in equal strain in the left and in the right gauge.

$$V_G = 5 \left(\frac{1 + K \cdot \epsilon_{bottom}}{2 + K \cdot (2\epsilon_{bottom})} - 0.5 \right) \tag{4.15}$$

$$V_G = 5 \left(\frac{1}{2} \frac{1 + K \cdot \epsilon_{bottom}}{1 + K \cdot (\epsilon_{bottom})} - 0.5 \right) \tag{4.16}$$

$$V_G = 0 \tag{4.17}$$

Twist then results in exactly opposite strain on both gauges, $\epsilon_{G,bottom} = -\epsilon_{G,top}$. In other words:

$$\epsilon_{bottom} = -\epsilon_{top} \tag{4.18}$$

$$\Delta\epsilon = \epsilon_{bottom} - \epsilon_{top} \tag{4.19}$$

$$\Delta\epsilon_{twist} = 2\epsilon_{bottom} = 2\epsilon_{top} \tag{4.20}$$

If we now insert this into equation 4.16 we get:

$$V_G = 5\left(\frac{1 + K \cdot \epsilon_{bottom}}{2 + K \cdot (\epsilon_{bottom} - \epsilon_{bottom})} - 0.5\right) \tag{4.21}$$

$$V_G = 5\left(\frac{1 + K \cdot \epsilon_{bottom}}{2} - 0.5\right) \tag{4.22}$$

$$\Delta\epsilon = \frac{4V_G}{5K} \tag{4.23}$$

Sources of error

Small deviations in alignment, outward position and K factor also result in a difference in measured strain. Because of these sources of error, in the flapping case there will be a sinusoidal signal at flapping frequency. Depending on whether the wing bending changes, the error might change $\Delta\epsilon$ between the two experimental conditions flapping (F) and flapping and rotating (F&R). To verify an increase/decrease in $\Delta\epsilon$ is caused by twist, the quarter bridge measurements can show to which extend bending has changed.

Data analysis

The experiments ran for 70 seconds. To ensure a constant sampling rate, the data is re-sampled at 1 kHz. Because of the re-sampling the first and last second of the dataset are discarded. Furthermore, because the rotation takes time to start up the sampling starts at t = 14 [s]. 10 sample windows of 5 seconds each were analyzed. For each 5 second sample, the Discrete Fourier transform is computed. The mean and standard deviation of the peak in the frequency domain are then compared between the different angular velocity conditions. Figure 4.9 gives an overview of how the experimental data is analyzed.

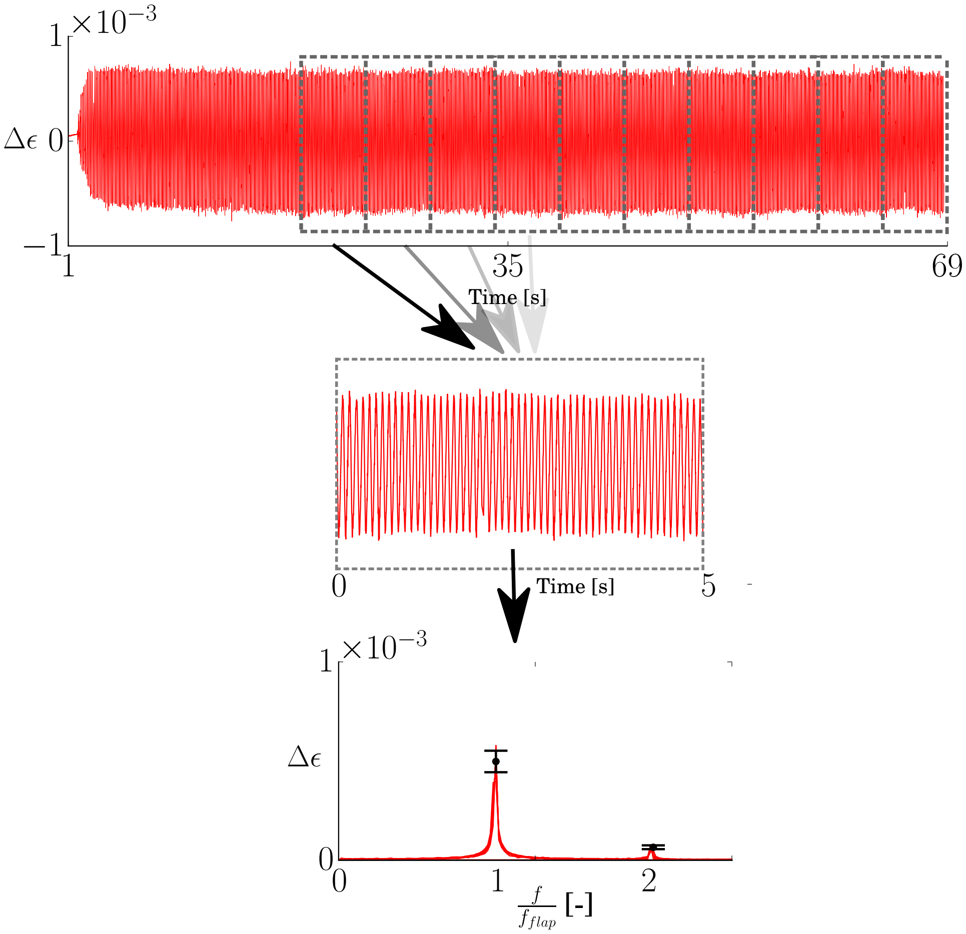

Figure 4.9: The measurements from an experiments is cut into 10 parts of 5 seconds each, then the discrete fourier transform is taken, and the peak values are averaged. Error bars show the standard deviation.

4.3 Wing eigenfrequency

A twisted wing release test was used to check the wing eigenfrequencies (figure 4.10). The first eigenfrequency is 22.5 Hz, the second eigenfrequency is found at 122.5 Hz. The first one is a first order bending, the second is likely to be the first twisting mode. If we look at the computed eigenfrequencies (figure 4.11), we see that they are quite a bit lower. This is likely because of slightly different material properties, and perpaps the stiffness added by the strain gauges and their wiring.

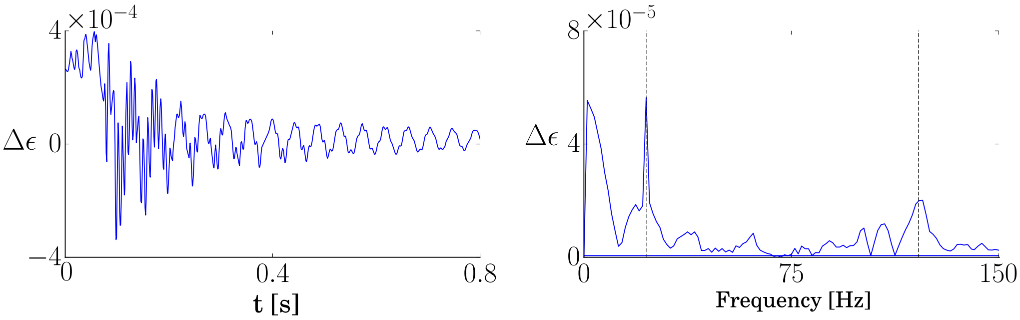

Figure 4.10: The difference in strain between the left and the right gauge after releasing a twisted wing position.

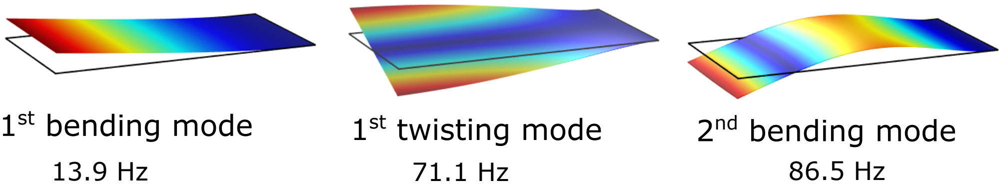

Figure 4.11: The eigenfrequencies of the wing computed with the finite element analysis.

Chapter 5

Results and discussion

In this chapter the results of the three methods are compared. The experiments are subdivided in those measured with quarter bridge and with half bridge configurations. The quarter bridge configuration results were normalized with the amplitude of the main bending strain to ensure no difference in strain due to bending is interpreted as twist. Figure 5.1 shows the effect of such a normalization. The results of the simulations and experiments are shown in figure 5.2. Because the quarter bridge results are not affected by a change in bending, the difference in $\Delta\epsilon$ as a result of inertial rotation is the result of wing twist. Table 5.1 gives an overview of the twist observed in simulations and experiments in case the result was significant.

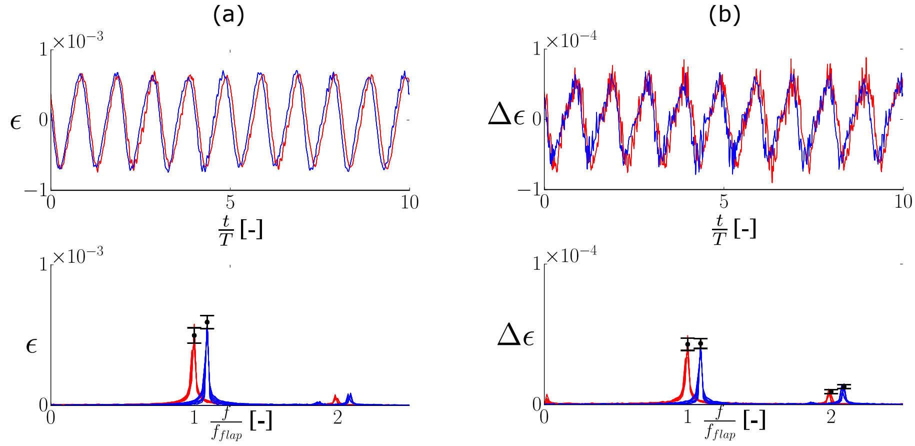

Figure 5.1: (a) The strain of a single strain gauge during 0 rps(red) and 3 rps (blue). (b) The difference between the left and the right gauge, calibrated with the difference in bending found from (a) The two signals in the frequency domain have been offset graphically by 0.1 on the horizontal axis for clarity.

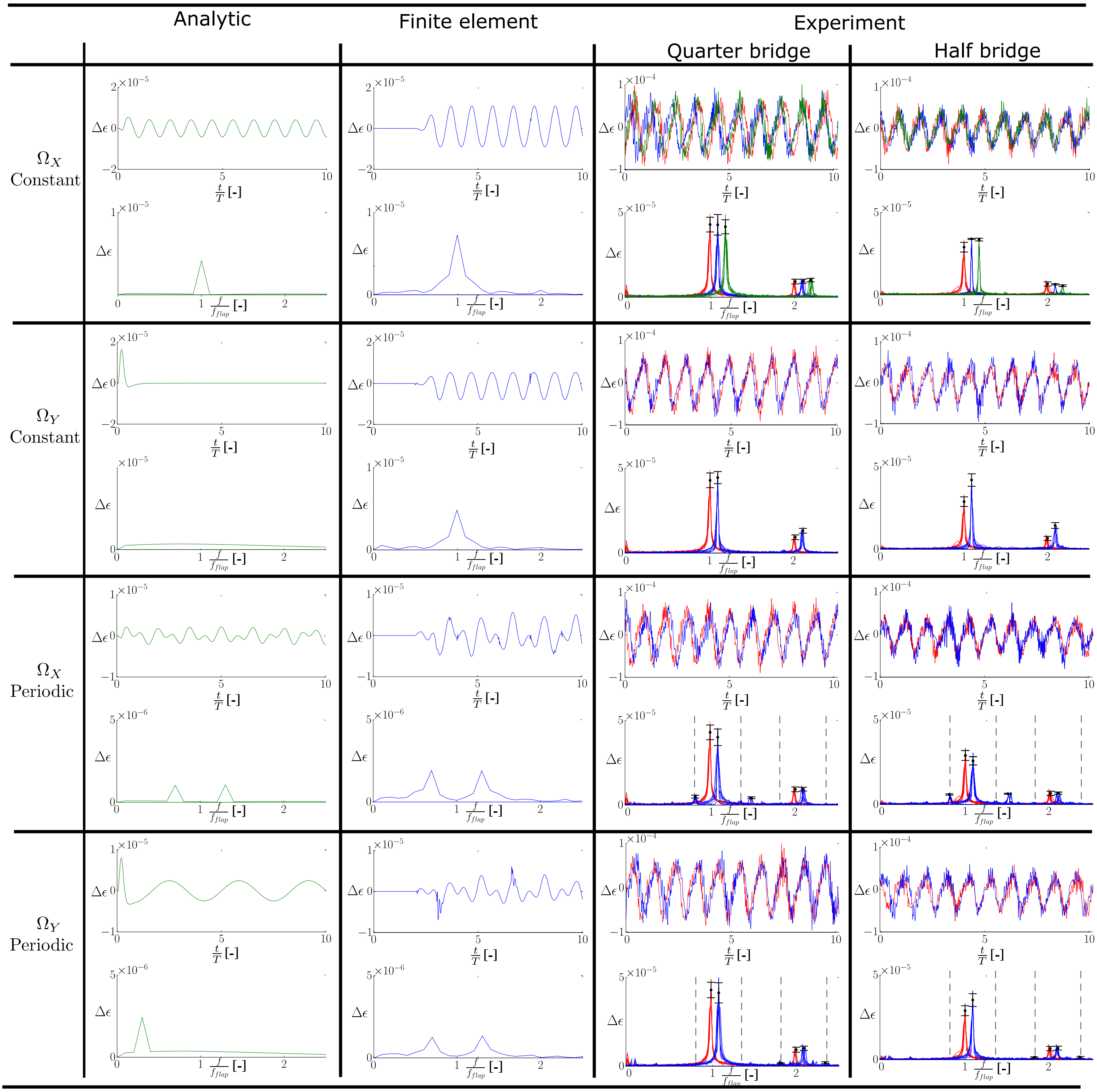

Figure 5.2: The results for the analytic Euler-Lagrange simulations, finite element simulations and the experiments with both wheatstone configurations. For all cases, the flapping frequency was 10 Hz, the angular velocity 3 rps, and the stroke amplitude 15 degrees. The experimental figures show 0 rps (red), 3 rps (blue), and in $\Omega_{X,const}$, 5 rps(green). The two signals in the frequency domain have been offset graphically by 0.1 on the horizontal axis for clarity. The experiments with periodic rotations have dashed lines to indicate $\frac{f_f \pm f_{rot}}{f_f}$ and $\frac{2f_f \pm f_{rot}}{f_f}$ frequencies.

5.1 Constant rotation

Both the analytic and finite element simulations show that the flapping wing will twist at the flapping frequency in case of Ω_X rotations. However, the magnitude of this twist is about twice as high in the Finite element results. This difference is not surprising considering the limitations of both models. Both predict $\Delta\epsilon$ in the order of $5 \cdot 10^{-6}$ at flapping frequency.

The experiments do not show a significant difference in the quarter bridge configuration. The half bridge experiments ostensibly show an increase in $\Delta\epsilon$ between 0 and 3 rps (red and blue), but not between 3 and 5 rps (blue and green). This is likely to be an artifact of the experimental setup. The average of the red column is lower and the spread of values is higher because the power in the frequency domain is spread over multiple adjacent frequencies. In the 3 and 5 rps results the spread is very low and the results from the Fourier transform are more accurate. Therefore, no $\Delta\epsilon$ can be distinguished experimentally in Ω_X rotations.

In the case of rotation around the Y axis, the finite element model again shows a twisting at flapping frequency, this time at a slightly smaller amplitude. The analytic model shows twist during the acceleration phase, but no response during constant rotation. When looking back at the derivation of the Euler-Lagrange model, we can indeed see that there is no dependence on constant rotation around Y (although angular accelerations around Y are noticeable). The derivation is limited by the shape functions that were used, and apparently these shape functions limit the relevance of the model to rotations around the X-axis.

The experiments for constant rotation in Ω_Y indicate twist at double the flapping frequency. The strain due to bending causes a $\Delta\epsilon$ that is compensated for in the quarter bridge results (see figure 5.1). The results from the half bridge setup can not be compensated this way, the increase in $\Delta\epsilon$ is thus mainly a result of an increase in bending.

5.2 Periodic rotation

During periodic rotations in Ω_X, the simulations and experiments are all in agreement. The signal contains two peaks near the flapping frequency, offset by ± the frequency of periodic rotation f_r. The amplitude of these peaks is more than two times larger in the experiments than observed in either simulation. This is likely caused by a difference in experimental parameters (e.g. material properties), and as described in section 4.2 the amplitude in the simulation results are likely to be inaccurate. Nonetheless, the values in table 5.1 show they are in the same order of magnitude.

The three different models are all in disagreement over the periodic rotations in Ω_Y. The analytic model can be disregarded because the derivation fails to incorporate Coriolis force in Ω_Y rotations. The finite element analysis shows similar results to periodic Ω_X

results, peaks around the flapping frequency. These are not found in the experiments. However, similar peaks around double flapping frequency are observed.

Table 5.1: The values of the frequency components in the analytic Euler-Lagrange analysis, the finite element simulations and the experiments. The experimental values are the averages of 10 measurement windows They have been corrected for an increase in bending. Only results with p<0.05 are shown. * p-value = $1.62 \cdot 10^{-5}$

Rotation	Analytic		Finite element		Experiment			
					Quarter bridge		Half bridge	
	frequency	$\Delta\epsilon$	frequency	$\Delta\epsilon$	frequency	$\Delta\epsilon$	frequency	$\Delta\epsilon$
Ω_X	f_f	$4.15 \cdot 10^{-6}$	f_f	$7.30 \cdot 10^{-6}$				
Ω_Y	f_f	0	f_f	$4.85 \cdot 10^{-6}$	$2 \cdot f_f$	$3.88 \cdot 10^{-6*}$		
Ω_X Periodic	$f_f \pm f_r$	$1.08 \cdot 10^{-6}$	$f_f \pm f_r$	$1.91 \cdot 10^{-6}$	$f_f - 2.92$	$5.03 \cdot 10^{-6}$	$f_f - 3.1$	$5.91 \cdot 10^{-6}$
					$f_f + 4.36$	$4.34 \cdot 10^{-6}$	$f_f + 4.5$	$6.36 \cdot 10^{-6}$
Ω_Y Periodic	f_r	$1.34 \cdot 10^{-6}$	$f_f \pm f_r$	$1.35 \cdot 10^{-6}$	$f_f - 2.9$	$1.59 \cdot 10^{-6}$	$f_f - 2.9$	$1.41 \cdot 10^{-6}$
					$f_f + 2.75$	$1.97 \cdot 10^{-6}$	$f_f + 3.2$	$1.8 \cdot 10^{-6}$

5.3 Evaluation of models

Although the Euler-Lagrange model proved effective in modeling rotations in Ω_X, it failed to incorporate Coriolis forces in Ω_Y rotations. Its use is therefore limited, although computations are much faster than the finite element analysis. The finite element simulations had issues with stability and convergence, but its results yielded similar results to the Euler-Lagrange models in Ω_X rotations. Runtime is quite significant at more than half an hour for one second of computation time.

The experiments proved how hard it is to detect small strain due to wing twist when a large bending signal is present. However, the experimental setup should be capable of detecting wing twist at the magnitudes that were predicted experimentally. The fact that many of the computational results for constant rotation were not observed experimentally is curious, especially since twist *was* observed in the periodic rotations

5.4 Recommendations

Because of a slightly fluctuating flapping frequency, the values of the peaks in the frequency domain are slightly lower than they would be in case of a perfectly constant flapping frequency. Furthermore, the hand-made wings introduced uncertainty in material properties and wing asymmetry. A redesigned experiment could solve these issues, this would be useful in determining the validity of the Euler-Lagrange and finite element analyses. However, the conclusions will not change with an improved setup. Wing twist remains exceedingly difficult to detect with two strain gauges.

The quarter Wheatstone bridge measurements turned out to be more valuable because it could identify a change in bending signal, as well as wing twist. Especially with a more accurate A/D chip the advantage of a half Wheatstone bridge is small. Detecting strain at various locations on the wing also could serve other purposes, next to detecting twist. Especially hovering animals or robots subjected to aerodynamic gusts, wing damage or flying in confined space could use wing strain information in control.

Conclusions and significance

Evidence of wing twist as a result of inertial rotation could be detected experimentally during all periodic rotations and during constant rotation around the Y-axis. However, in both simulations and experiments the strain due to wing twist is exceedingly small compared to the strain due to bending. Wing twist thus remains very difficult to observe experimentally, and simulations of flapping flat plates generally differed from experimental observations.

A flapping wing is able to sense some types of inertial rotations with the limited setup of two strain gauges. However, detecting inertial rotation turned out to be very challenging with this setup. Hawk moths and other insects have many more sensors on their wings. Considering the challenges in detecting wing twist, an array of sensors would be a more viable way to detect inertial rotations.

Furthermore, it turns out wing twist is not the only parameter that indicates inertial rotation. Strain due to wing bending increased significantly during Ω_Y rotations. An increased bending is not unique to body rotations, but a richly sensed wing might be able to distinguish different load cases such as increased aerodynamic load or altered stroke amplitude.

The hind wings of the ancestral flies must have had some sensory function, however small, for them to evolve into these optimized haltere structures. The hawk moth wing with its hundreds of sensors will have some sensory function, otherwise the redundant campaniforms would have degraded over its long evolutionary history. The fact that twist can be measured in robotic wings means it is likely hawk moth wings can sense this as well. This gives a hint to how the evolution of halteres might have started, and perhaps on how the haltere functions today.

This research focused very narrowly on two sensors during body rotations, hypothesizing twist is the best mechanism to detect rotations. By broadening the scope of sensing by flapping wings, other mechanisms and functionalities are likely to emerge. There is potential for future research to embrace machine-learning algorithms in determining flight states from a richly sensed wing. This could change the paradigm to a less deterministic way of biology research, and introduce a new way of looking at biology-inspired engineering.

References

[1] Aono, H., Liang, F., and Liu, H. Near-and far-field aerodynamics in insect hovering flight: an integrated computational study. *Journal of Experimental Biology*, 211(2):239–257, 2008.

[2] Bender, J. A. and Dickinson, M. H. A comparison of visual and haltere-mediated feedback in the control of body saccades in drosophila melanogaster. *Journal of Experimental Biology*, 209(23):4597–4606, 2006.

[3] Birch, J. M. and Dickinson, M. H. Spanwise flow and the attachment of the leading-edge vortex on insect wings. *Nature*, 412(6848):729–733, 2001.

[4] Birch, J. M. and Dickinson, M. H. The influence of wing–wake interactions on the production of aerodynamic forces in flapping flight. *Journal of Experimental Biology*, 206(13):2257–2272, 2003.

[5] Bomphrey, R. J., Taylor, G. K., and Thomas, A. L. Smoke visualization of free-flying bumblebees indicates independent leading-edge vortices on each wing pair. In *Animal Locomotion*, pages 249–259. Springer, 2010.

[6] Chan, W. P., Prete, F., and Dickinson, M. H. Visual input to the efferent control system of a fly's" gyroscope". *Science*, 280(5361):289–292, 1998.

[7] Combes, S. and Daniel, T. Flexural stiffness in insect wings i. scaling and the influence of wing venation. *Journal of experimental biology*, 206(17):2979–2987, 2003.

[8] Combes, S. A. and Daniel, T. L. Into thin air: contributions of aerodynamic and inertial-elastic forces to wing bending in the hawkmoth manduca sexta. *Journal of Experimental Biology*, 206(17):2999–3006, 2003.

[9] Dickerson, B. H., Aldworth, Z. N., and Daniel, T. L. Control of moth flight posture is mediated by wing mechanosensory feedback. *The Journal of experimental biology*, pages jeb–103770, 2014.

[10] Dickinson, M. H. Comparison of encoding properties of campaniform sensilla on the fly wing. *Journal of Experimental Biology*, 151(1):245–261, 1990.

[11] Dickinson, M. H. Haltere–mediated equilibrium reflexes of the fruit fly, drosophila melanogaster. *Philosophical Transactions of the Royal Society of London. Series B: Biological Sciences*, 354(1385):903–916, 1999.

[12] Dickinson, M. H., Lehmann, F.-O., and Sane, S. P. Wing rotation and the aerodynamic basis of insect flight. *Science*, 284(5422):1954–1960, 1999.

[13] Dombrowski, U. J. Untersuchungen zur funktionellen organisation des flugsystems von manduca sexta (l). 1991.

[14] Droogendijk, H., Brookhuis, R., de Boer, M., Sanders, R., and Krijnen, G. Towards a biomimetic gyroscope inspired by the fly's haltere using microelectromechanical systems technology. *Journal of the Royal Society interface*, 11(99):20140573, 2014.

[15] Dyhr, J. P., Morgansen, K. A., Daniel, T. L., and Cowan, N. J. Flexible strategies for flight control: an active role for the abdomen. *The Journal of experimental biology*, 216(9):1523–1536, 2013.

[16] Eberle, A., Dickerson, B., Reinhall, P., and Daniel, T. A new twist on gyroscopic sensing: body rotations lead to torsion in flapping, flexing insect wings. *Journal of The Royal Society Interface*, 12(104):20141088, 2015.

[17] Ellington, C. The aerodynamics of hovering insect flight. v. a vortex theory. *Philosophical Transactions of the Royal Society of London. B, Biological Sciences*, pages 115–144, 1984.

[18] Ellington, C. P., Van Den Berg, C., Willmott, A. P., and Thomas, A. L. Leading-edge vortices in insect flight. 1996.

[19] Frye, M. A. Behavioral neurobiology: a vibrating gyroscope controls fly steering maneuvers. *Current biology*, 17(4):R134–R136, 2007.

[20] Gnatzy, W., Grünert, U., and Bender, M. Campaniform sensilla of calliphora vicina (insecta, diptera). *Zoomorphology*, 106(5):312–319, 1987.

[21] Hedrick, T. and Daniel, T. Flight control in the hawkmoth manduca sexta: the inverse problem of hovering. *The journal of experimental Biology*, 209(16):3114–3130, 2006.

[22] Hinson, B. T. and Morgan, K. A. Gyroscopic sensing in the wings of the hawkmoth manduca sexta: the role of sensor location and directional sensitivity. In *Bioinspiration & Biomimetics (forthcoming)*, 2015.

[23] Hinson, B. T., Rombokas, E., Dyhr, J. P., Daniel, T. L., and Morgansen, K. A. Sensing from control: Airframe deformation for simultaneous actuation and state estimation. In *Decision and Control (CDC), 2013 IEEE 52nd Annual Conference on*, pages 2683–2690. IEEE, 2013.

[24] Hinterwirth, A. J. and Daniel, T. L. Antennae in the hawkmoth manduca sexta (lepidoptera, sphingidae) mediate abdominal flexion in response to mechanical stimuli. *Journal of Comparative Physiology A*, 196(12):947–956, 2010.

[25] Hinterwirth, A. J., Medina, B., Lockey, J., Otten, D., Voldman, J., Lang, J. H., Hildebrand, J. G., and Daniel, T. L. Wireless stimulation of antennal muscles in freely flying hawkmoths leads to flight path changes. *PloS one*, 7(12):e52725, 2012.

[26] Jongerius, S. and Lentink, D. Structural analysis of a dragonfly wing. *Experimental Mechanics*, 50(9):1323–1334, 2010.

[27] Keil, T. A. Functional morphology of insect mechanoreceptors. *Microscopy research and technique*, 39(6):506–531, 1997.

[28] Kramer, v. M. Die zunahme des maximalauftriebes von tragflugeln bei plotzlicher anstellwinkelvergrosserung (boeneffekt). *Z. Flugtech. Motorluftschiff*, 23:185–189, 1932.

[29] Land, M. F. and Collett, T. Chasing behaviour of houseflies (fannia canicularis). *Journal of comparative physiology*, 89(4):331–357, 1974.

[30] Liu, H. and Aono, H. Size effects on insect hovering aerodynamics: an integrated computational study. *Bioinspiration & Biomimetics*, 4(1):015002, 2009.

[31] Liu, H., Ellington, C. P., Kawachi, K., Van Den Berg, C., and Willmott, A. P. A computational fluid dynamic study of hawkmoth hovering. *The journal of experimental biology*, 201(4):461–477, 1998.

[32] Liu, H. and Kawachi, K. A numerical study of insect flight. *Journal of Computational Physics*, 146(1):124–156, 1998.

[33] MATLAB. *version 7.10.0 (R2010a).* The MathWorks Inc., Natick, Massachusetts, 2010.

[34] Muijres, F., Johansson, L., Barfield, R., Wolf, M., Spedding, G., and Hedenström, A. Leading-edge vortex improves lift in slow-flying bats. *Science*, 319(5867):1250–1253, 2008.

[35] Multiphysics, C. *version 5.1.* COMSOL, Inc., Burlington, Massachusetts, 2015.

[36] Nalbach, G. The halteres of the blowfly calliphora. *Journal of Comparative Physiology A*, 173(3):293–300, 1993.

[37] Norris, A. G., Palazotto, A. N., and Cobb, R. G. Structural dynamic characterization of an insect wing. In *Proceedings of the 51st AIAA/ASME/ASCE/AHS/ASC Structures, Structural Dynamics, and Materials Conference*, 2010.

[38] Pittaway, A. et al. *The hawkmoths of the western Palaearctic.* Harley books, 1993.

[39] Pringle, J. Proprioception in insects ii. the action of the campaniform sensilla on the legs. *Journal of Experimental Biology*, 15(1):114–131, 1938.

[40] Pringle, J. W. S. The gyroscopic mechanism of the halteres of diptera. *Philosophical Transactions of the Royal Society of London. Series B, Biological Sciences*, pages 347–384, 1948.

[41] Sane, S. P. and Dickinson, M. H. The aerodynamic effects of wing rotation and a revised quasi-steady model of flapping flight. *Journal of Experimental Biology*, 205(8):1087–1096, 2002.

[42] Sane, S. P., Dieudonné, A., Willis, M. A., and Daniel, T. L. Antennal mechanosensors mediate flight control in moths. *Science*, 315(5813):863–866, 2007.

[43] Sherman, A. and Dickinson, M. H. A comparison of visual and haltere-mediated equilibrium reflexes in the fruit fly drosophila melanogaster. *Journal of Experimental Biology*, 206(2):295–302, 2003.

[44] Sherman, A. and Dickinson, M. H. Summation of visual and mechanosensory feedback in drosophila flight control. *Journal of Experimental Biology*, 207(1):133–142, 2004.

[45] Shyy, W., Aono, H., Kang, C.-k., and Liu, H. *An introduction to flapping wing aerodynamics*, volume 37. Cambridge University Press, 2013.

[46] Snider, S. B., Yuste, R., and Packer, A. M. A neural circuit for angular velocity computation. *Frontiers in neural circuits*, 4, 2010.

[47] Sreenivasamurthy, S. and Ramamurti, V. Coriolis effect on the vibration of flat rotating low aspect ratio cantilever plates. *The Journal of Strain Analysis for Engineering Design*, 16(2):97–106, 1981.

[48] Theobald, J. C., Warrant, E. J., and O'Carroll, D. C. Wide-field motion tuning in nocturnal hawkmoths. *Proceedings of the Royal Society B: Biological Sciences*, 277(1683):853–860, 2010.

[49] Thompson, R., Wehling, M., Evers, J., and Dixon, W. Evaluation of the haltere as a biologically inspired inertial rate measurement sensor. In *Guidance, Navigation, and Control Conference*, 2008.

[50] Thompson, R., Wehling, M., Evers, J., and Dixon, W. Body rate decoupling using haltere mid-stroke measurements for inertial flight stabilization in diptera. *Journal of Comparative Physiology A*, 195(1):99–112, 2009.

[51] Videler, J., Stamhuis, E., and Povel, G. Leading-edge vortex lifts swifts. *Science*, 306(5703):1960–1962, 2004.

[52] Warrick, D. R., Tobalske, B. W., and Powers, D. R. Lift production in the hovering hummingbird. *Proceedings of the Royal Society of London B: Biological Sciences*, 276(1674):3747–3752, 2009.

[53] Weis-Fogh, T. Energetics of hovering flight in hummingbirds and in drosophila. *Journal of Experimental Biology*, 56(1):79–104, 1972.

[54] Willmott, A. P. and Ellington, C. P. The mechanics of flight in the hawkmoth manduca sexta. i. kinematics of hovering and forward flight. *Journal of Experimental Biology*, 200(21):2705–2722, 1997.

[55] Wootton, R. J. Functional morphology of insect wings. *Annual review of entomology*, 37(1):113–140, 1992.

[56] Wu, G. and Zeng, L. Measuring the kinematics of a free-flying hawk-moth (macroglossum stellatarum) by a comb-fringe projection method. *Acta Mechanica Sinica*, 26(1):67–71, 2010.

[57] Wu, W. C., Wood, R. J., and Fearing, R. S. Halteres for the micromechanical flying insect. In *Robotics and Automation, 2002. Proceedings. ICRA'02. IEEE International Conference on*, volume 1, pages 60–65. IEEE, 2002.

[58] Zhao, L., Huang, Q., Deng, X., and Sane, S. P. Aerodynamic effects of flexibility in flapping wings. *Journal of The Royal Society Interface*, page rsif20090200, 2009.

[59] Zill, S. and Moran, D. T. The exoskeleton and insect proprioception. i. responses of tibial campaniform sensilla to external and muscle-generated forces in the american cockroach, periplaneta americana. *Journal of Experimental Biology*, 91(1):1–24, 1981.

Appendices

A Coriolis force derivation

The Coriolis force is a fictitious force, it is caused by Newton's first law that states that an object will continue to move in a straight line unless a force is acting upon it. The term Coriolis force is often associated with meteorology, veering moving particles on the Northern Hemisphere to the right, and to the left on the southern Hemisphere. The Coriolis force can be described by looking at the inertial (I) and the rotating (R) reference frame. In the inertial frame, the frame of reference is static, and one can draw the analogy of an observer looking at a static window. In the rotational frame however, the frame of reference moves with $\omega(t)$.

In the inertial frame (figure 3a), vector **a** can be separated in a radial and a tangential component. In the rotating frame (figure 3b), only the radial component is visible. Therefore the transformation between inertial and rotating requires taking into account the tangential component: a_t, or $\omega \times r$.

$$\mathbf{a} = a_r + a_t \tag{1}$$

$$\mathbf{a} = a_r + \omega \times r \tag{2}$$

If we now imagine vector a to be a velocity $\frac{d\mathbf{r}}{dt}$ we get:

$$\frac{d\mathbf{r}}{dt}|_I = \left.\frac{d\mathbf{r}}{dt}\right|_R + \boldsymbol{\omega} \times \mathbf{r} \tag{3}$$

If we are now interested in accelerations in the inertial frame, we again have differentiated w.r.t. the inertial reference frame:

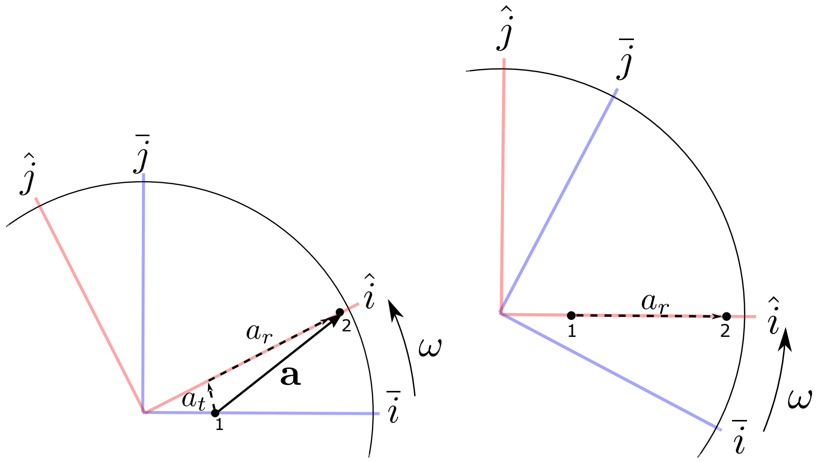

(a) Inertial frame

(b) Rotating frame

Figure 3: The inertial and rotating frame for a two dimensional vector **a** from point 1 to point 2. In the inertial frame, **a** can be constructed by a radial and tangential component. In the rotating frame, vector a_r spans point 1 to point 1. Here we must take into account that the frame has rotated with ω.

$$\left.\frac{d\left(\frac{d\mathbf{r}}{dt}\right)}{dt}\right|_I = \left.\frac{d\left(\frac{d\mathbf{r}}{dt}\right)}{dt}\right|_R + \boldsymbol{\omega}\times\left(\frac{d\mathbf{r}}{dt}\right) \tag{4}$$

$$\left.\frac{d\left(\frac{d\mathbf{r}}{dt}\right)}{dt}\right|_I = \left.\frac{d\left(\frac{d\mathbf{r}}{dt}\big|_R + \boldsymbol{\omega}\times\mathbf{r}\right)}{dt}\right|_R + \boldsymbol{\omega}\times\left(\left.\frac{d\mathbf{r}}{dt}\right|_R + \boldsymbol{\omega}\times\mathbf{r}\right) \tag{5}$$

$$\left.\frac{d\left(\frac{d\mathbf{r}}{dt}\right)}{dt}\right|_I = \left.\frac{d\left(\frac{d\mathbf{r}}{dt}\right)}{dt}\right|_R + \frac{d\boldsymbol{\omega}}{dt}\times\mathbf{r} + \boldsymbol{\omega}\times\left.\frac{d\mathbf{r}}{dt}\right|_R + \boldsymbol{\omega}\times\left.\frac{d\mathbf{r}}{dt}\right|_R + \boldsymbol{\omega}\times(\omega\times\mathbf{r}) \tag{6}$$

The individual terms have names:

$$\mathbf{F}_{Inertial} = \underbrace{m\frac{d^2\mathbf{r}}{dt^2}|_R}_{Linear\ acceleration} + \underbrace{m\frac{d\boldsymbol{\omega}}{dt}\times\mathbf{r}}_{Angular\ acceleration} + \underbrace{2m\boldsymbol{\omega}\times\frac{d\mathbf{r}}{dt}|_R}_{Coriolis\ force} + \underbrace{m\boldsymbol{\omega}\times(\boldsymbol{\omega}\times\mathbf{r})}_{Centrifugal\ force} \tag{7}$$

We can now rewrite the forces in the rotating reference frame (in this case, there are no external forces, $\mathbf{F}_{Inertial} = 0$):

$$\underbrace{\frac{d^2\mathbf{r}}{dt^2}|_R}_{Linear\ acceleration} = -\underbrace{\frac{d\boldsymbol{\omega}}{dt}\times\mathbf{r}}_{Angular\ acceleration} - \underbrace{2\boldsymbol{\omega}\times\frac{d\mathbf{r}}{dt}|_R}_{Coriolis\ acceleration} - \underbrace{\boldsymbol{\omega}\times(\boldsymbol{\omega}\times\mathbf{r})}_{Centrifugal\ acceleration} \tag{8}$$

B Euler-Lagrange derivation

$$L = T - V \tag{9}$$

If we define the integral in time of that Lagrangean we get the total work done by the system S.

$$S = \int_{t_1}^{t_2} L(t, q_1, \dot{q_1})dt \tag{10}$$

Now we want to find the minimum of S, but first we substitute q with g.

$$g_\epsilon = q(t) + \epsilon\eta(t) \tag{11}$$

This gives us:

$$\frac{dS}{d\epsilon} = \int_{t_1}^{t_2} \frac{L_\epsilon}{d\epsilon}dt \tag{12}$$

$$\frac{dS}{d\epsilon} = \int_{t_1}^{t_2} (\frac{dL_\epsilon}{dg_\epsilon}\eta + \frac{dL_\epsilon}{dg'_\epsilon}\eta')dt \tag{13}$$

We now take ϵ to ben an extremely small value. (g becomes q). Furthermore, no work is done by the system.

$$0 = \int_{t_1}^{t_2} (\frac{dL_\epsilon}{dq'}\eta' + \frac{dL_\epsilon}{dq}\eta)dt \tag{14}$$

Applying integration by parts to the latter part of the equation, with $\frac{dL(t_1)}{dq'} = \frac{dL(t_2)}{dq'}$ because of

$$0 = \int_{t_1}^{t_2} (\frac{dL}{dq}\eta)dt + \eta\frac{dL}{dq'}]_{t1}^{t2} - \int_{t_1}^{t_2} (\eta\frac{d}{dt}\frac{dL}{dq'})dt \tag{15}$$

$$0 = \eta\int_{t_1}^{t_2} (\frac{dL}{dq} - \frac{d}{dt}\frac{dL}{dq'})dt \tag{16}$$

$$0 = \frac{dL}{dq} - \frac{d}{dt}\frac{dL}{dq'} \tag{17}$$

Now we have the formulation to build up the equations of motion (note, q can also be a vector of generalized coordinates). We can now insert the decomposition of L ($L = T - V$). Instead of defining no external work done, we can include a term Q_i. This term could also include external forces

$$\frac{d}{dt}(\frac{\partial L}{\partial \dot{q}_i}) - \frac{\partial L}{\partial q_i} = Q_i \tag{18}$$

$$\frac{d}{dt}(\frac{\partial (T-V)}{\partial \dot{q}_i}) - \frac{\partial (T-V)}{\partial q_i} = Q_i \tag{19}$$

Now separating out the terms, we have no potential energy terms depend on $\dot{q}$. Note that T depends on q_i, unlike most Lagrange derivations that have a single mass matrix and a single springlike component.

$$\frac{d}{dt}(\frac{\partial (T-V)}{\partial \dot{q}_i}) - \frac{\partial (T-V)}{\partial q_i} = Q_i \tag{20}$$

$$\frac{d}{dt}(\frac{\partial (T)}{\partial \dot{q}_i}) - \frac{\partial (T)}{\partial q_i} - \underbrace{\frac{d}{dt}(\frac{\partial (V)}{\partial \dot{q}_i})}_{=0} + \frac{\partial (V)}{\partial q_i} = Q_i \tag{21}$$

$$\frac{d}{dt}(\frac{\partial (T)}{\partial \dot{q}_i}) - \frac{\partial (T)}{\partial q_i} + \frac{\partial (V)}{\partial q_i} = Q_i \tag{22}$$

C Digital supplement

The digital supplement containing the data, the code used in the experiments and analysis can be found on github:

`https://github.com/tlmohren/Msc_thesis.git`

The supplement contains a folder with results (Data), a folder with the Euler-Lagrange implementation in MATLAB, a folder with python scripts used to analyze experimental results, and the schematic for the printed circuit board in EAGLE 7.2.0, CadSoft, Pines, Florida, 2015 (`PCB_design`).

- `Data`
  - `Comsol_mesh_convergence` (4 .CSV files)
  - `Comsol_simulations` (9 .CSV files)
  - `flapping_data_10_04` (26 .CSV files)
  - `Matlab_simulations` (8 .mat files)
- `Matlab`
  - `Aerodynamic_force_estimate`
  - `Euler_Lagrange_simulation`
    - `runsimulations`
    - `flappermodel_rotvect`
    - `createODEfile_rotvect`
    - `funcCa`
    - `PlateODE`
    - `shape2`
    - `shapefunc2`
- `Python`
  - `Compare_quarter_half`
  - `data_analysis_10_04_halfbridge`
  - `data_analysis_10_04_quarterbridge`
  - `eigenfrequency_analysis`
  - `Force_simulation`
  - `Mesh_convergence_analysis`
  - `Simulation_analysis`
  - `thesis_functions`
- `PCB_design`
  - `amp_shield_v2.3 (.pdf, .brd, .sch)`